



## RESEARCH ARTICLE

10.1029/2022JD037907

### Key Points:

- The largest stratopause trend is found in the Southern Hemisphere polar region during austral spring based on Microwave Limb Sounder observations
- The suppression of gravity waves in UA-ICON reveals the importance of resolved waves and their ability to compensate missing drag
- In the polar regions, the simulated stratopause is too warm and the tropical semi-annual oscillation is about two months out of phase

### Correspondence to:

K. Karami,  
[khalil.karami@uni-leipzig.de](mailto:khalil.karami@uni-leipzig.de)

### Citation:

Karami, K., Borchert, S., Eichinger, R., Jacobi, C., Kuchar, A., Mehrdad, S., et al. (2023). The climatology of elevated stratopause events in the UA-ICON model and the contribution of gravity waves. *Journal of Geophysical Research: Atmospheres*, 128, e2022JD037907. <https://doi.org/10.1029/2022JD037907>

Received 22 SEP 2022  
Accepted 30 MAR 2023




### Author Contributions:

**Conceptualization:** Khalil Karami  
**Data curation:** Khalil Karami  
**Formal analysis:** Khalil Karami, Sebastian Borchert, Roland Eichinger, Christoph Jacobi, Ales Kuchar, Petr Pisoft, Petr Sacha  
**Investigation:** Khalil Karami, Roland Eichinger, Christoph Jacobi, Ales Kuchar, Sina Mehrdad, Petr Pisoft, Petr Sacha  
**Methodology:** Khalil Karami, Roland Eichinger, Christoph Jacobi, Ales Kuchar, Sina Mehrdad, Petr Pisoft, Petr Sacha  
**Resources:** Khalil Karami  
**Software:** Khalil Karami, Sebastian Borchert, Sina Mehrdad  
**Supervision:** Khalil Karami, Sebastian Borchert, Christoph Jacobi

© 2023. The Authors.

This is an open access article under the terms of the [Creative Commons Attribution License](https://creativecommons.org/licenses/by/4.0/), which permits use, distribution and reproduction in any medium, provided the original work is properly cited.

# The Climatology of Elevated Stratopause Events in the UA-ICON Model and the Contribution of Gravity Waves

Khalil Karami<sup>1</sup> , Sebastian Borchert<sup>2</sup>, Roland Eichinger<sup>3,4</sup>, Christoph Jacobi<sup>1</sup> , Ales Kuchar<sup>1</sup>, Sina Mehrdad<sup>1</sup>, Petr Pisoft<sup>4</sup> , and Petr Sacha<sup>4</sup>

<sup>1</sup>Institute for Meteorology, Leipzig University, Leipzig, Germany, <sup>2</sup>Deutscher Wetterdienst, Offenbach am Main, Germany, <sup>3</sup>Deutsches Zentrum für Luft- und Raumfahrt (DLR), Berlin, Germany, <sup>4</sup>Faculty of Mathematics and Physics, Charles University, Prague, Czech Republic

**Abstract** The climatologies of the stratopause height and temperature in the UA-ICON model are examined by comparing them to 17-years (2005–2021) of Microwave Limb Sounder (MLS) observations. In addition, the elevated stratopause (ES) event occurrence, their main characteristics, and driving mechanisms in the UA-ICON model are examined using three 30-year time-slice experiments. While UA-ICON reasonably simulates the large-scale stratopause properties similar to MLS observations, at polar latitudes in the Southern Hemisphere the stratopause is ~8 K warmer and ~3 km higher than observed. A time lag of about two months also exists in the occurrence of the tropical semiannual oscillation of the stratopause compared to the observations. ES events occur in ~20% of the boreal winters, after major sudden stratospheric warmings (SSWs). Compared to the SSWs not followed by ES events (SSW-only), the ES events are associated with the persistent tropospheric forcing and prolonged anomalies of the stratospheric jet. Our modeling results suggest that the contributions of both gravity waves (GWs) and resolved waves are important in explaining the enhanced residual circulation following ES events compared to the SSW-only events but their contributions vary through the lifetime of ES events. We emphasize the role of the resolved wave drag in the ES formation as in the sensitivity test when the non-orographic GW drag is absent, the anomalously enhanced resolved wave forcing in the mesosphere gives rise to the formation of the elevated stratopause at about 85 km.

**Plain Language Summary** Using 17 years (2005–2021) of Microwave Limb Sounder (MLS) observations, we show negative (cooling stratopause temperatures and decreasing stratopause heights) trends in most regions and seasons. The largest negative trend in the stratopause temperature (by considering all regions and all seasons) is found in the Southern Hemisphere (SH)'s polar region during austral spring. The seasonal average of cooling rates is comparable in the mid-latitudes of Northern Hemisphere and SH. In the UA-ICON simulations, the elevated stratopause events (ESEs) occur after major sudden stratospheric warmings (SSWs). ESEs frequency is 2 events per decade in UA-ICON simulations. Our results show that the wind reversal is stronger and long-lasting in the ESEs compared to SSW-only events. In addition, the easterlies extend to the mesosphere in the composites of ESEs, but the reversed winds are limited to below 60 km in the case of SSW-only events. We show that the non-orographic gravity wave drag induces anomalous residual circulation after SSW that causes the ESEs. We also show that the ESEs form even in the absence of non-orographic gravity wave drag. In this case, the anomalous residual circulation is due to the anomalously enhanced resolved wave forcing in the mesosphere that gives rise to the formation of the ESEs at about 85 km.

## 1. Introduction

The upper boundary of the stratosphere, the stratopause, is sensitive to the increasing concentrations of greenhouse gases (GHG) and is considered an independent and novel indicator of GHG-induced climate change (Olivero & Thomas, 2001; Pisoft et al., 2021; Rind et al., 1998). Both space- and ground-based observations indicate a robust stratospheric temperature decrease of about 1–3 K over the last four decades (1979–2018, Steiner et al. (2020a)), including a near-global cooling near the stratopause (Steiner et al., 2020b). Associated with such a temperature decrease, Pisoft et al. (2021) estimated a global decrease in stratopause height and stratospheric thickness for the future climate under increasing concentration of GHG. Stratopause height trends are crucial to correctly understand and attribute changes in dynamics and tracer transport, and moreover, they may affect satellite orbits (Schröder et al., 2007). It is therefore of interest to study the characteristics of the stratopause (e.g., its height and temperature) and understand the mechanisms influencing it. While in low and mid-latitudes, the

**Validation:** Khalil Karami, Roland Eichinger, Christoph Jacobi, Ales Kuchar, Sina Mehrdad, Petr Pisoft, Petr Sacha  
**Visualization:** Khalil Karami, Ales Kuchar  
**Writing – original draft:** Khalil Karami  
**Writing – review & editing:** Khalil Karami, Sebastian Borchert, Roland Eichinger, Christoph Jacobi, Ales Kuchar, Sina Mehrdad, Petr Pisoft, Petr Sacha

stratopause is found at about 50 km and is maintained by absorption of shortwave radiation by ozone, in the polar night region it is maintained by the warming induced by the descending branch of the gravity wave (GW) driven mesospheric residual circulation (Garcia & Boville, 1994; Hitchman et al., 1989). The polar winter stratopause is generally warmer and is located at higher altitudes ( $\approx 60$  km) than in the mid-latitudes (France & Harvey, 2013; Kanzawa, 1989). Under undisturbed or quiet wintertime conditions, planetary waves that carry westward momentum break approximately near the critical levels (e.g., the zero-wind line) in the low latitude stratosphere or in the high latitude mesosphere. On the other hand, the prevailing westerly zonal flow in the stratosphere blocks most of the eastward propagating GWs allowing only the westward propagating GWs to reach the mesosphere where they dissipate between 60 and 80 km and deposit momentum toward their direction of propagation which in turn slows down the prevailing zonal flow and induces a poleward and downward meridional circulation below the breaking level in the winter polar region that helps to maintain the warm winter stratopause (Chandran et al., 2014; de la Torre et al., 2012; Limpasuvan et al., 2016). This “separated” stratopause happens in both hemispheres, but is more persistent and pronounced in the Southern Hemisphere (SH) winter (Hitchman et al., 1989).

Under disturbed stratospheric polar vortex conditions, however, the conditions for the propagation of planetary waves (PWs) and GWs are significantly altered. The reversal of the zonal wind that characterizes major sudden stratospheric warmings (SSW) prevents further upward propagation of large-scale PWs into the stratosphere and also alters the propagation conditions of orographic GWs and westward-propagating non-orographic GWs into the mesosphere. Therefore, following the SSW onset with an atypical wintertime GW filtering, only eastward propagating GWs are permitted to penetrate to the winter mesosphere/lower thermosphere (MLT) region (Holton, 1983; Siskind et al., 2010). This provides eastward drag that induces an equatorward and upward mean meridional circulation in the high-latitude mesosphere (similar to the summer conditions) that leads to a cooling of the upper polar mesosphere (de Wit et al., 2014; Liu & Roble, 2002; Thurairajah et al., 2014; Yamashita et al., 2010). Such a temperature structure is referred to as a mesospheric inversion layer (Garcia & Boville, 1994; Sassi et al., 2002). Following an SSW, in general, an almost isothermal stratosphere and ill-defined stratopause forms (Manney et al., 2008). After an SSW onset, the unstable easterly polar stratospheric jet generates the so-called *secondary PWs* due to the presence of instabilities which leads to a strong westward PW drag above 80 km (Chandran, Garcia, et al., 2013).

The westward PW forcing is stronger than the eastward GW forcing in the mesosphere following an SSW, which initiates a poleward and downward mean meridional circulation over the winter pole. On the other hand, the eastward zonal mean flow is re-established at higher altitudes earlier than the lower stratospheric winds, as the thermal relaxation in the upper mesosphere can be two to three times faster than in the lower stratosphere (Wehrbein & Leovy, 1982). During the recovery of the eastward zonal winds in the mesosphere and upper stratosphere and the reestablishment of the polar vortex, a new stratopause forms at considerably higher altitudes ( $\approx 80$  km) than its mean climatological values ( $\approx 50$ – $60$  km). This is known as an elevated stratopause (ES; Labitzke (1972); Manney et al. (2005)) event. Not all SSWs are followed by an ES event (ESE). Chandran, Collins, et al. (2013) identified 2–4 ESEs occurring each decade in the Whole Atmospheric Community Climate Model (WACCM) which was about half the frequency of SSWs (de la Torre et al., 2012). Chandran, Collins, et al. (2013) also reported that the GW forcing in the MLT region and the anomalous residual circulations remain reversed for a longer period during ESEs compared to SSWs that do not generate ESEs.

Understanding the coupling between the stratosphere and the MLT during ESEs can provide insights into the understanding of energy transfer in the middle atmosphere (Yigit & Medvedev, 2016). In addition, as the downward branch of the mean meridional circulation is located at a higher altitude during the reestablishment of the stratopause in ES events, mesospheric air can intrude into the stratosphere and influences the chemistry of the stratosphere, which is important in chemistry-climate models because it indirectly affects the dynamics of the stratosphere (Siskind et al., 2015). Mesospheric air is characterized by a low concentration of water vapor, high concentrations of CO and reactive odd nitrogen ( $\text{NO}_x = \text{NO} + \text{NO}_2$ ) (Orsolini et al., 2010; Randall et al., 2009; Siskind et al., 2007). The downward transport of  $\text{NO}_x$  into the stratosphere can catalyze the destruction of ozone (Randall et al., 2005). The magnitude of the secondary ozone layer (90–95 km) during mesospheric cooling decreases, and the altitude of the tertiary ozone maximum (70–75 km) also drops (Kvissel et al., 2012; Smith et al., 2009; Tweedy et al., 2013).

Understanding the details of ESEs using reanalysis data has its own limitations as the upper lid of most reanalyses is around or below 0.01 hPa ( $\approx 80$  km). Also in the presence of the sponge layer in reanalyses to damp

upward-propagating waves near the model top to limit reflections from the upper boundary, a detailed study of the role of PWs and GWs is difficult. For example, Manney et al. (2008) have shown that MERRA reanalyses are unable to capture the rise of the stratopause to very high altitudes during ESEs. With the improvements in the spatial and temporal resolutions of middle and upper atmospheric satellite data, detailed analyses of ESEs have become feasible in recent years (France, Harvey, Alexander, et al., 2012; Manney et al., 2008; Naren Athreyas et al., 2022; Orsolini et al., 2010; Shi et al., 2022). Modeling studies with WACCM (France & Harvey, 2013; Limpasuvan et al., 2016; Orsolini et al., 2017), the Canadian Middle Atmosphere Model (CMAM; McLandress et al., 2013), a high-resolution middle atmosphere GCM developed for the KANTO project (Tomikawa et al., 2012), the ECHAM/MESy Atmospheric Chemistry (EMAC; Scheffler et al., 2022) and with the Japanese Atmospheric General circulation model for Upper Atmosphere Research (JAGUAR, Okui et al. (2021)) provided insights into the sequence of events associated with the occurrence of a typical ES event. For example, Limpasuvan et al. (2016) using WACCM showed that while PWs are important at the onset of ESEs, GWs are crucial in explaining the residual circulation before and after ESEs. However, using the same model Chandran, Collins, et al. (2013) found that the enhancement of PW forcing is not present in all ES cases. In other words, they showed that in WACCM simulations, there exist ESEs whose entire process of formation is due to the actions of GWs, although this might be model dependent.

Therefore, the relative contributions of GWs and PWs in the formation of ESEs are still under discussion and remain to be elucidated. The goal of the present study is to investigate in detail the climatology of the stratopause and the ESEs occurrence, their main characteristics, and driving mechanisms in the UA-ICON model and compare it with a 17-year climatology (2005–2021) based on Microwave Limb Sounder (MLS) observations. The paper is organized as follows: Section 2 describes the UA-ICON simulations as well as analysis methods. Section 3 describes the main characteristics of stratopause and ESEs in the UA-ICON model and MLS observations and finally, in Section 4, we summarize the major findings.

## 2. UA-ICON Simulations, MLS Observations, and Analysis Methods

### 2.1. UA-ICON Setup and Simulations

The ICON model is a joint project by the German Weather Service (DWD) and the Max Planck Institute for Meteorology, aiming at providing a unified modeling system to seamlessly allow simulations from climatological time scales to large-eddy simulations as well as for global and local numerical weather prediction (Zängl et al., 2015). ICON has one single dynamical core, but with respect to the physics parameterizations, there are two different main configurations. One is intended for numerical weather prediction (ICON-NWP, Zängl et al. (2015)), and the other one was developed for use in climate research (ICON-A, Giorgetta et al. (2018)). In our study, we employ the ICON version 2.6.3 as distributed by the DWD. This version allows to combine the upper-atmosphere physics (UA-ICON) with ICON-NWP, but not with ICON-A. Therefore, we used basically a numerical weather prediction setup for our simulations. For simulations including the upper atmosphere, the dynamical core can be switched from shallow to deep atmosphere dynamics (Borchert et al., 2019). In our setup of the ICON model, we used a global R2B4 grid, which is a horizontal grid with a mesh size of approximately 160 km. For the vertical grid, we use 120 layers up to a model top at about 150 km altitude (the vertical grid is stretched, with layer thicknesses increasing from bottom to model top). The time step of all simulations is 360s except for one experiment (see Section 2.1 below) and the data output interval was set to 6 hr. We note at this place that the NWP setup is not particularly tuned for such relatively coarse horizontal grid resolutions and for time scales that significantly extend beyond the synoptic time scale. Therefore, some degree of degradation is possible in our simulations. The mid-monthly sea surface temperature (SST) and sea ice concentration (SIC) values produced by the Program for Climate Model Diagnosis and Intercomparison (PCMDI) for the Atmosphere Model Intercomparison Project (AMIP, (Taylor et al., 2000)) served as lower boundary condition data. The concentrations of CO<sub>2</sub>, CH<sub>4</sub>, N<sub>2</sub>O, CFC-11, and CFC-12 were taken from the historical greenhouse gas volume mixing ratios for CMIP6 (Meinshausen et al., 2017). The atmospheric ozone concentrations were prescribed based on the input4MIPs project (<https://esgf-node.llnl.gov/search/input4mips>). The period of simulation is 1980–2015 (hereafter, CLIM) and is used to evaluate the UA-ICON model with the satellite observations. An evaluation of the parameterization of upper-atmosphere physics in UA-ICON is presented in Borchert et al. (2019) for a global R2B4 grid, and the sensitivity of the general circulation to the missing GW parameterization using the same grid are presented in Karami et al. (2022). Köhler et al. (2021) suggested an adjustment of the GW drag parameterization in ICON, in order to improve the stratospheric circulation in the NH winter. We adopt this adjustment for the current study.

In addition to the CLIM simulation, we performed a set of 30-year long time-slice experiments with the UA-ICON model by employing repeated annual cycles of SST, SIC, and greenhouse gases of the year 1985. This year was selected as both El-Niño southern oscillation and Pacific decadal oscillation were in their neutral phase and no explosive volcano eruption has occurred; hence conditions in this year can serve as a useful proxy for the multi-year mean conditions and an estimate of their internal variability. First, a control (CTL) simulation was carried out where both the sub-grid scale orography (SSO) scheme and non-orographic GW scheme are used and two sensitivity tests where (a) the SSO scheme was disabled (no-SSO, hereafter) and (b) the non-orographic GW scheme was disabled (no-GWD, hereafter). Although the exclusion of GW drags results in a very strong forcing, this kind of simulation has been performed previously using other models (e.g., EMAC (Eichinger et al. (2020)), WACCM (Kuilman & Karlsson, 2018) and CMAM (Ren et al., 2011)) and has been shown to be useful in understanding the importance of GW drags for middle atmospheric dynamics. In ICON, the SSO drag is treated after Lott and Miller (1997), and the non-orographic GW drag parameterization that treats the generation, propagation, and breaking of GWs from synoptic-scale flow (e.g., fronts, convection, jet streams) is based on the works of Warner and McIntyre (1996) and Scinocca (2003). In ICON model the minimum and maximum intrinsic phase speeds for the non-orographic gravity waves are 0.25 and 100  $\text{ms}^{-1}$ , respectively. Further details including the description of the scheme for computing the horizontal wind and temperature tendencies can be found in ECMWF (2018). The time step of the CTL and no-SSO simulations was 360s but it was reduced to 120s in the no-GWD simulation. In the no-GWD simulation, the winds in the upper stratosphere and mesosphere were too strong which lead to the violation of the Courant-Friedrichs-Lewy (CFL) condition. Reducing the time step to 120s (compared to the 360s in CTL simulation) solved this issue.

## 2.2. MLS Satellite Observations

MLS is an Earth observation instrument onboard NASA's Aura satellite with a 705 km sun-synchronous orbit and orbital period of 100 min (Waters et al., 2006). An atmospheric limb scan is performed every 25 s and therefore MLS is able to sample about 3500 profiles each day that are spaced 165 km along the satellite track covering the latitude range from 82°S to 82°N (Waters et al., 2006). While MLS observes thermal emissions from the atmospheric limb on five frequencies (118, 190, 240, and 640 GHz and 2.5 THz), the temperature and geopotential height profiles are inferred from 118 to 240 GHz oxygen emissions from the surface up to 120 km. For the current study, we use Level 3 daily binned temperature and geopotential height on assorted grids version 4 of MLS data (Schwartz et al., 2020) from 2005 to 2021.

## 2.3. Analysis Method

The available MLS temperature data are provided on pressure levels. In order to compare the stratopause characteristics in MLS with UA-ICON simulations, we follow the approach presented by France, Harvey, Alexander, et al. (2012). First, we interpolate MLS temperatures from pressure to geometric altitudes (using MLS geopotential data) from 10 to 120 km at 1 km increments. In the case of UA-ICON outputs, this is easier as UA-ICON is a model on height levels and we simply interpolate the model output from 10 to 120 km at 1 km increments. Although, the stratopause is typically defined as a level where the temperature maximizes in the middle atmosphere, however, multiple local temperature maxima may occur particularly at high latitudes in the case of SSWs, deep isothermal layers, mesospheric inversion layers, and even noise in the temperature profiles which makes the “true” or “actual” stratopause difficult to identify in such conditions. Hence, to identify the stratopause the following procedure was applied for each vertical temperature profile. First, we smoothed each temperature profile by applying an 11 km boxcar averaging, and then the temperature maximum ( $T_{\text{max}}$ ) was identified between 20 and 85 km with the condition that the lapse rate at the five adjacent 1 km increment levels must be negative above  $T_{\text{max}}$  and positive below  $T_{\text{max}}$ . Afterward, 15 km above and below of the height of  $T_{\text{max}}$  in the smoothed profile was used to search for the maximum temperature in the unsmoothed profile. The temperature and altitude of  $T_{\text{max}}$  in the unsmoothed profile was considered as the actual stratopause. In case these conditions are not met, the stratopause was not defined in the given temperature profile and this case was excluded from the calculation of stratopause climatology.

Here, we only consider major SSWs according to the World Meteorological Organization (WMO) criterion, that is, simultaneous reversal of the zonal mean zonal wind at 60°N and the zonal mean temperature gradient between 60°N and 90°N at 10 hPa from November to April (Labitzke, 1981a). The westerlies at 10 hPa and 60°N must

persist at least for 14 consecutive days before a new SSW event can be identified. The stratospheric final warmings are excluded by requiring 21 consecutive days of westerlies at 10 hPa and 60°N before 30 April. Based on these criteria, the frequency of SSW in the CTL run is 5.7 events per decade which is in good agreement with the reanalysis data with a frequency of approximately six events per decade (Charlton & Polvani, 2007). As mentioned earlier, after the onset of SSW events the stratopause becomes ill-defined and therefore the following method is used to identify ESEs. To mitigate the spurious variability of the stratopause height during and after the onset of SSWs, France and Harvey (2013) computed the average polar cap (70°–90°N) stratopause height for days 3–7 prior to each day (Z<sup>-</sup>) and 3–7 days following each day (Z<sup>+</sup>) and considered ES event candidates when the difference between Z<sup>+</sup> and Z<sup>-</sup> exceeds 10 km. After determining ES candidates, the “actual” ES event onset is identified as the first day when the daily mean stratopause height jumps by at least 25 km compared to the previous day. In the case of UA-ICON, the 25 km threshold results in too few ESEs and therefore we reduced this threshold to 18 km. Nevertheless, even with the reduced threshold, we found approximately two ESEs per decade in UA-ICON (CTL simulation) which is less than the observed frequency of ESEs (3.5 events per decade in MLS observations (Naren Athreya et al., 2022)). The annual frequency of ESEs was reported between 28% and 36% in four 53-year simulations by WACCM (Chandran, Collins, et al., 2013). Recently, Scheffler et al. (2022) reported that with a threshold value for the stratopause height jump of 8.4 km, the ES frequency is 2.4 events per decade in a free-running EMAC simulation. It is worthwhile to mention that it is possible to increase the frequency of ESEs in UA-ICON by reducing the threshold of the vertical displacement of the stratopause height, but here we select the 18 km threshold as it identifies the strongest or “true” ESEs in the mid-winter in UA-ICON. Note that after some SSWs the stratopause descends to lower altitudes and then suddenly reforms at higher altitudes (at least 18 km based on our algorithm), however, the altitudes of such ESEs are comparable to the altitudes of the stratopause prior to SSW occurrence. Therefore, the “true or strongest” ESEs refer to those ESEs that the reformed ES altitude is at least 10 km higher than the average pre-SSW (21 days prior to the SSW occurrence day) stratopause heights. A composite map of different fields around the occurrence of ESEs for the CTL simulation and comparison with the sensitivity runs helps to figure out the importance of GWs in the formation of ESEs. The statistical significance of differences between the CTL run and sensitivity tests in stratopause properties is determined with the Student's *t*-test at a 99% level. In addition, for the comparison between ESEs and SSWs not followed by ESEs, we use *p*-values to highlight the regions where the fields significantly differ from each other.

### 3. Stratopause Properties in the UA-ICON Model and the Contribution of Gravity Waves

#### 3.1. MLS Stratopause Trend

Figure 1 shows the scatter plot of stratopause temperature (thick black dots) using 17 years (2005–2021) of MLS observations, its variability (represented by the standard deviation and shown by the light gray error bars), and the linear regression lines (blue and red lines represent the negative and positive trends, respectively). The years with a major SSW in the Northern Hemisphere (NH) are denoted by the red crosses. Quantification of the change rates of stratopause temperature (slope of linear regression in K/year multiplied by the 17 years, which are shown by  $\Delta T$  in each panel) allows a more straightforward interpretation of the stratopause temperature trends in different seasons and regions. Except for a few seasons or regions with positive trends (red regression lines), the stratopause temperature trends, in general, indicate negative (cooling) trends in most regions and seasons. While the seasonal average of cooling rates are comparable in the mid-latitudes of the NH and SH ( $\Delta T = -1.86$  K, and  $\Delta T = -1.63$  K, respectively), the SH polar region has experienced the largest cooling rate ( $\Delta T = -1.87$  K) compared to the NH counterpart ( $\Delta T = -0.62$  K). The largest negative trend (by considering all regions and all seasons) is found in the SH polar region in SON ( $\Delta T = -4.06$  K). The largest cooling trend (by considering all regions) is found in the SON season, where the magnitude of the average temperature change in 17 years of MLS stratopause temperature data is  $\Delta T = -1.75$  K. Figure 2 shows the same information as Figure 1 but for the stratopause height. Similar to the trends in the stratopause temperature, there are a few exceptions that the stratopause height indicates a positive trend. However, generally, a negative (decreasing) trend in the stratopause height is found in most regions and seasons. There is no one-to-one relationship between the stratopause height and temperature trends in the MLS observations, but the stratopause cooling and reduction in the stratopause heights are found in most seasons and regions. The cooling rate and their magnitudes are comparable to those reported by Pisoft et al. (2021) who used data from state-of-the-art coupled chemistry-climate models and showed that the stratospheric extent has declined by 400m between 1980 and 2018.

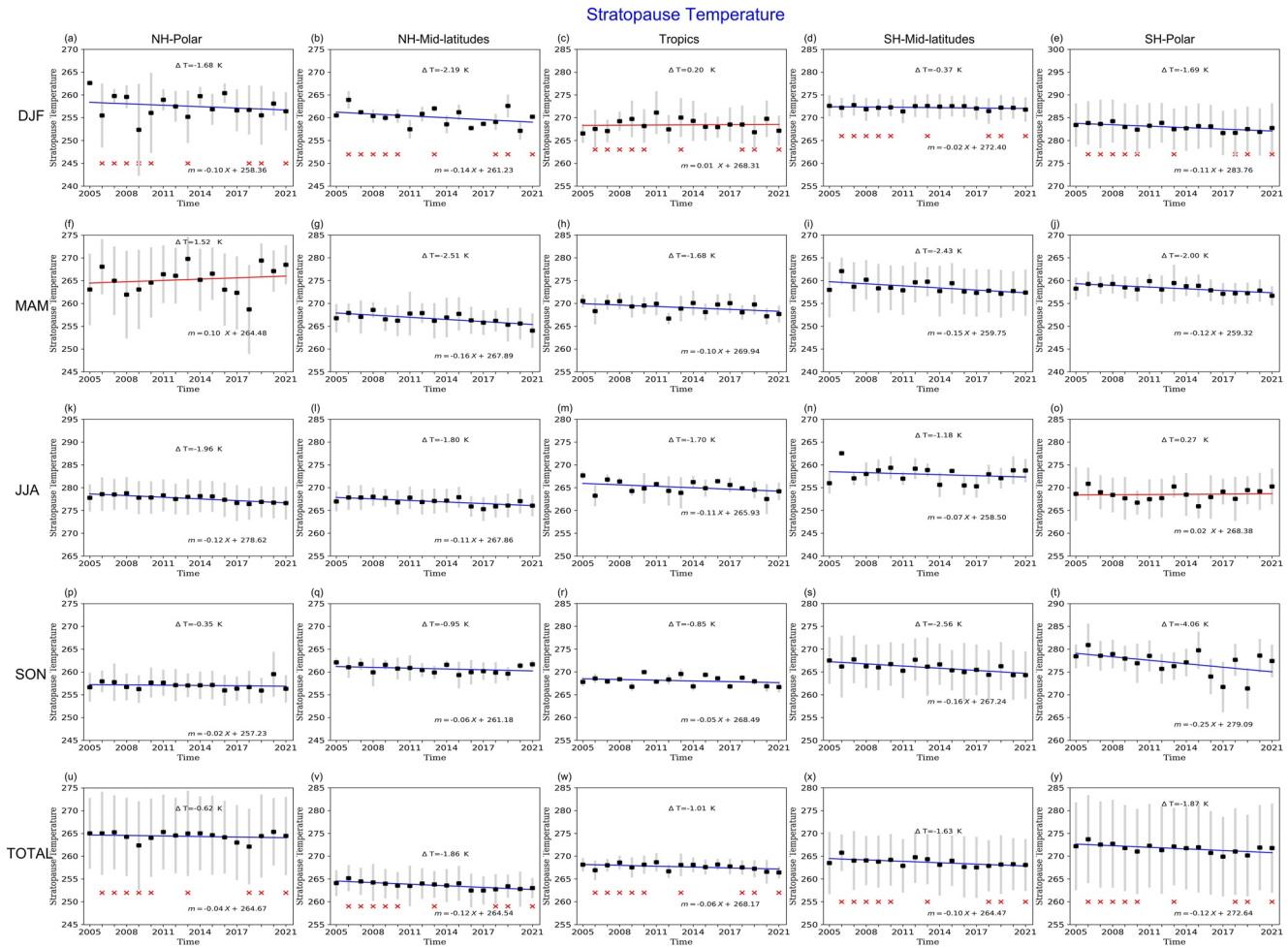


**Figure 1.** Time series of stratopause temperatures using 17 years of MLS observations in different seasons and regions (60°N–80°N for the Northern Hemisphere (NH) polar region (a, f, k, p, and u), 28°N–52°N for the NH mid-latitudes (b, g, l, q, and v), 8°S–8°N for the tropical region (c, h, m, r, and w), 28°S–52°S for the Southern Hemisphere (SH) mid-latitudes (d, i, n, s, and x), and 60°S–80°S for the SH polar region (e, j, o, t, and y)). The thick black dots are the mean values of the stratopause temperature for a given year, and the blue and red lines are the linear regression lines for the positive and negative trends, respectively. The light gray error bars are the standard deviation of the stratopause temperatures for a given year. The red crosses indicate the years with a major SSW during the DJF season. The seasons are defined as: the months of December (previous year), January, and February (DJF), the months of March, April, and May (MAM), the months of June, July, and August (JJA), and months of September, October, and November (SON). The total stratopause temperature change during the time series is calculated by multiplying the linear slope by the number of years under study (17 years).

### 3.2. Stratopause Climatology in UA-ICON

In Figure 3, the annual cycle of stratopause temperature for MLS measurements and the CLIM simulation from UA-ICON is depicted in terms of latitude–time evolution. In general, UA-ICON (CLIM) replicates MLS measurements in both hemispheres for large-scale stratopause temperature features such as the warm polar summer stratopause and the cold midwinter stratopause (Barnett, 1974; France, Harvey, Randall, et al., 2012). The semiannual oscillation of the tropical stratopause is caused by seasonal variations in the solar zenith angle and the amount of insolation. The tropical semi-annual oscillation is also fairly simulated, which is consistent with (France, Harvey, Randall, et al., 2012; Hitchman & Leovy, 1986; Hood, 1986). The UA-ICON (CLIM) stratopause temperatures have less seasonal variability (less than 5 K) in the tropics than at higher latitudes (about 25 and 35 K in the NH and SH, respectively), which is consistent with the MLS findings. This is due to the fact that low latitudes receive constant daytime sunlight. The GW-driven descent and hence warming in the polar region interrupts the cold winter stratopause which is more evident in the SH where the lowest stratopause temperature in MLS are found between 45° and 60°S rather than at southern polar latitudes. This feature is missing in UA-ICON (CLIM) where the minimum temperature is found further poleward at approximately 80°S in early winter. This is the largest

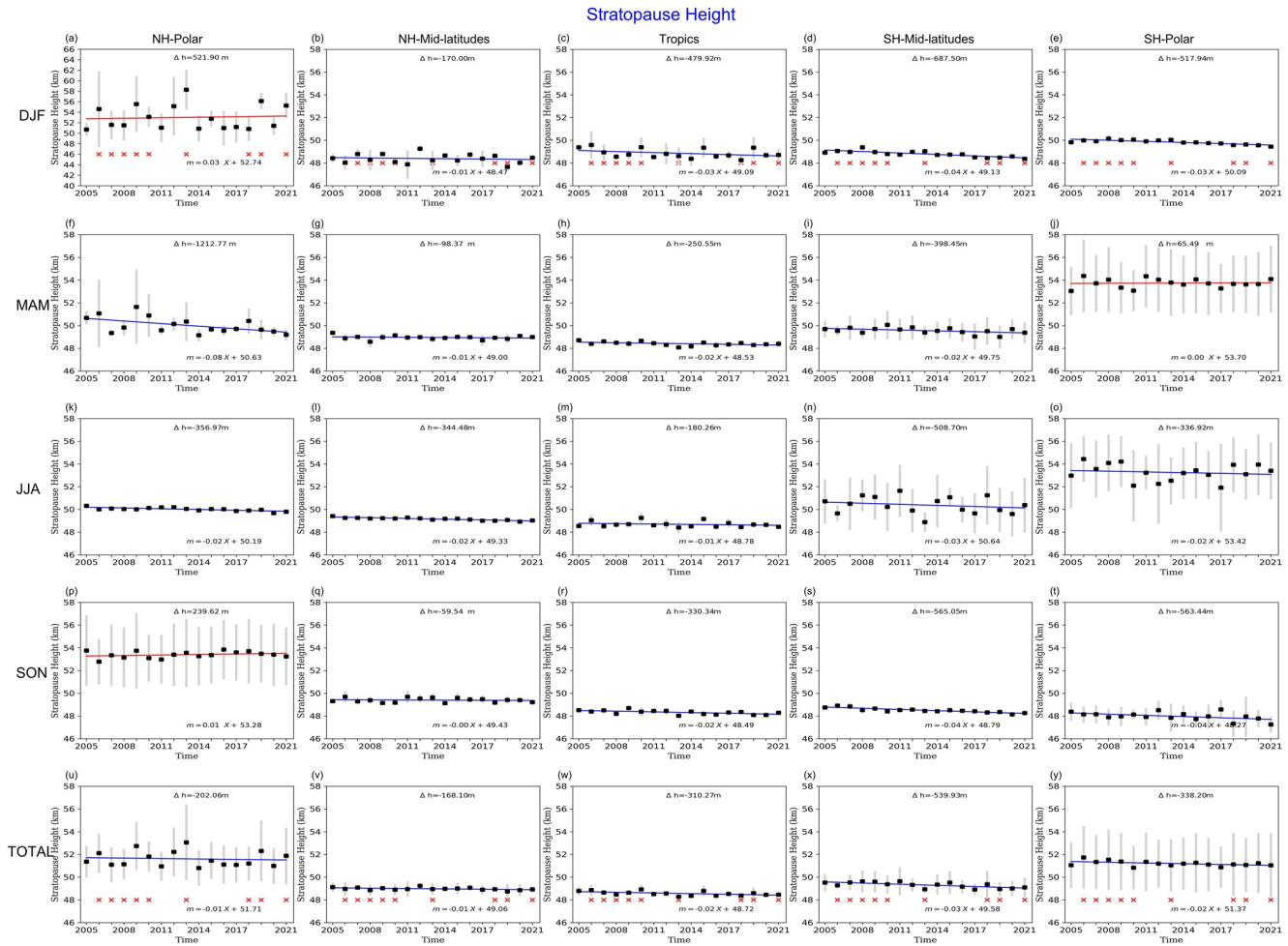
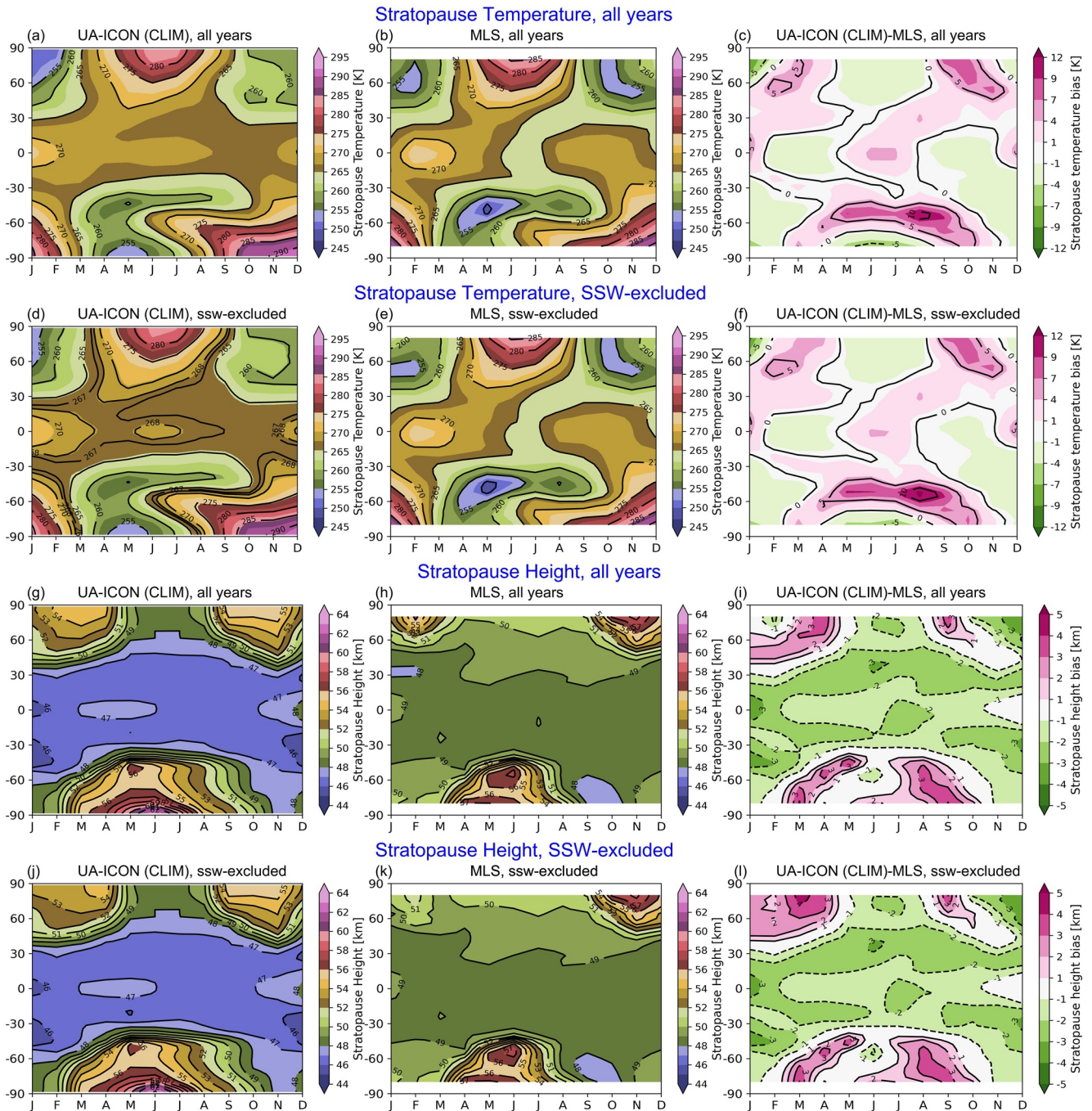


Figure 2. The same as Figure 1 but for the stratopause height.

discrepancy between the UA-ICON (CTL) simulation and MLS observations (Figure 3c). The mesospheric cooling associated with the SSWs yields a less coherent warm anomaly associated with the GW-driven descent in the NH (France, Harvey, Randall, et al., 2012; Garcia & Boville, 1994; Labitzke, 1981b), and this feature of the stratopause temperature, in general, is well-reproduced in UA-ICON (CLIM) in the NH. The major differences between MLS observations and the UA-ICON (CLIM) simulation are shown in Figure 3 (right column). While the polar-separated stratopause (poleward of 60°N) in midwinter (from December to February) in the NH matches well with the MLS observations, the stratopause is approximately 6 and 8K warmer in UA-ICON (CLIM) during spring and autumn equinoxes, respectively (Figure 3c). In the SH, UA-ICON (CLIM) stratopause temperatures are warming up to 8 K around 60°S throughout the cold months (May-September, Figure 3f). In the tropics, from December to January and also from June to July the UA-ICON (CLIM) stratopause temperatures are up to 4 K warmer than MLS and about 2 K colder than MLS from February to March (Figure 3c).

Similar to Figure 3 (left), the latitude-time plots of the annual cycle of stratopause height for MLS observations and UA-ICON simulation (CLIM) are shown in Figure 3 (middle). As for the stratopause temperature patterns, in general, the UA-ICON (CLIM) realistically reproduces the large-scale features of the stratopause height compared to MLS observations. In the tropics and mid-latitudes of both hemispheres, the stratopause is mostly located about 1–3 km lower than seen in the MLS observations. While the semiannual oscillation of stratopause height is present in UA-ICON (CLIM), its timing differs from the MLS observations as the maximum stratopause heights are found in January-February and July-August in MLS observations but in UA-ICON the local maximums of tropical stratopause heights are found in March-June and November-December periods in the UA-ICON (CLIM). Due to a lower solar zenith angle and higher altitude of maximum solar heating, the stratopause heights



**Figure 3.** Latitude-time plot of the average annual cycle of stratopause temperature (a–f) and stratopause height (g–l). The annual cycles in UA-ICON are based on the CLIM simulation (1980–2015) and in MLS data (middle column) are based on 2005–2021 satellite data. The right column shows differences between UA-ICON and MLS. The second and fourth row shows seasonal cycles after excluding years with SSW.

rise toward the winter solstice in both hemispheres (France, Harvey, Randall, et al., 2012). The polar stratopause descends in the spring due to the Sun's return to greater zenith angles, and as a result, the summer months in both hemispheres have the lowest stratopause heights. Since ascending can cool and raise the stratopause and descent can warm and lower it, there is an anti-correlation between the stratopause's height and its temperature. The comparison between MLS observations and UA-ICON (CLIM) simulation of the stratopause height is presented in Figure 3i. In the NH, while the stratopause in the UA-ICON (CLIM) simulation in high latitudes is about 2–3 km lower than in the MLS observations in winter (November–February) and summer (May–August), it is



up to 4 km higher in spring (March to May) and autumn (September–October, Figure 3i). In the SH, except for a short period (November–January), the stratopause heights in the UA-ICON (CLIM) are higher than in the MLS observations in mid and higher latitudes (Figure 3i).

The climatology of the stratopause temperatures in the CTL, no-SSO and no-GWD simulations and the impact of the exclusion of GWs on the stratopause temperatures are shown in Figure 4 (left column). In response to absence of SSO drag in the NH (Figure 4g), a weak ( $\approx 2$  K) but statistically significant stratopause temperature reduction is found in mid-latitudes from January to April, and in high-latitudes, a strong (up to 10 K) but statistically insignificant warming is found. The high-latitude warming in the SH from July to November is weaker than the NH counterpart but it is statistically significant. The mid-latitude stratopause temperature reduction is also statistically significant from March to September in the SH. Figure 4i shows the impact of absence of non-orographic gravity wave drag (GWD) on the stratopause temperature. In general, the responses are statistically significant everywhere and every time except in high-latitudes of NH during winter, spring, and summer. The amplitude of the upward propagating PWs are large in the middle and upper stratosphere during the NH winter. The perturbed forcings in the GW parametrization drag might be compensated/canceled by the resolved large-scale wave driving of opposite sign through the so-called compensation mechanism which alongside with large variability might explain the insignificant change in stratopause temperature in NH winter (Eichinger et al., 2020; Karami et al., 2022). In the NH during autumn equinox a negative (up to 20 K colder) and statistically significant response can be seen. In the SH, the impact of missing GWD manifests itself in the statistically significant colder (up to 20 K) stratopause from March to October. The stratopause in high latitudes is warmer in the summer season both in the NH and SH, but only the differences in the SH are statistically significant. While the absence of SSO has negligible impact on the stratopause temperature in tropical latitudes, the absence of GWD leads to a colder stratopause throughout the annual cycle. While in the no-SSO simulation, positive (warming) temperatures are found during cold months in both NH and SH, missing GWD causes cooling in the same period and in both hemispheres. The missing SSO drag leads to an accelerated stratospheric polar vortex up to 20 and 5  $\text{ms}^{-1}$  in the NH and SH, respectively during cold seasons (not shown). This causes more filtering of the eastward-propagating non-orographic GWs in the stratosphere or anomalously strong westward GW drag in the high-latitude mesosphere in no-SSO simulation compared to the CTL, which drives an anomalously stronger clockwise (poleward and downward) circulation in the mesosphere that gives rise to the stratopause warmings in the high-latitudes of both hemispheres. Conversely, the missing GWD in the no-GWD simulation leads to anomalously weak westward drag in the mesosphere compared to the CTL simulation (not shown) giving rise to the anti-clockwise (equatorward and upward) circulation in the mesosphere that causes a colder and higher stratopause in the no-GWD simulation.

Similar to the stratopause temperature, the climatology of the stratopause heights in the CTL, noSSO and noGWD simulations and the impact of absence of GWs on the stratopause heights are shown in Figure 4 (right column). While the magnitudes of the responses in the stratopause heights due to the absence of SSO drag (Figure 4h) are comparable in the NH and SH, only the responses in the SH are statistically significant. Similar to the effects on the stratopause temperature, the exclusion of nonorographic GW drag leads to statistically significant changes in most areas and throughout the seasonal cycle in the SH. In general, the response of the stratopause heights to absence of GWD (Figure 4j) are statistically significant in the SH and in low-latitudes of NH throughout the seasonal cycle. In general, the stratopause temperature and height responses to absence of GWD are consistent, for instance in the high-latitude SH that the elevated stratopause due to the absence of GWD is accompanied by the colder stratopause.

### 3.3. Elevated Stratopause Events in UA-ICON

It is of interest to first analyze the UA-ICON model simulations in reproducing the known features of SSWs and ESEs. Table 1 presents the statistics of major SSWs, ESEs, and also SSWs not followed by ESEs in the UA-ICON CTL simulation and sensitivity runs. In UA-ICON, ESEs occur after major SSWs. The frequency of SSWs is reduced in both the no-SSO and no-GWD runs with a more pronounced reduction in the no-SSO simulation. Therefore in response to missing GWs, the frequency of ESEs is reduced in both runs but our algorithm detects four ESEs in both sensitivities runs. In the CTL simulation, the ESEs are detected between 5 and 19 days following SSW events (the average value is 11 days). On average, the ESEs are detected 14 and 12 days following SSW events in the noSSO and noGWD simulations, respectively.

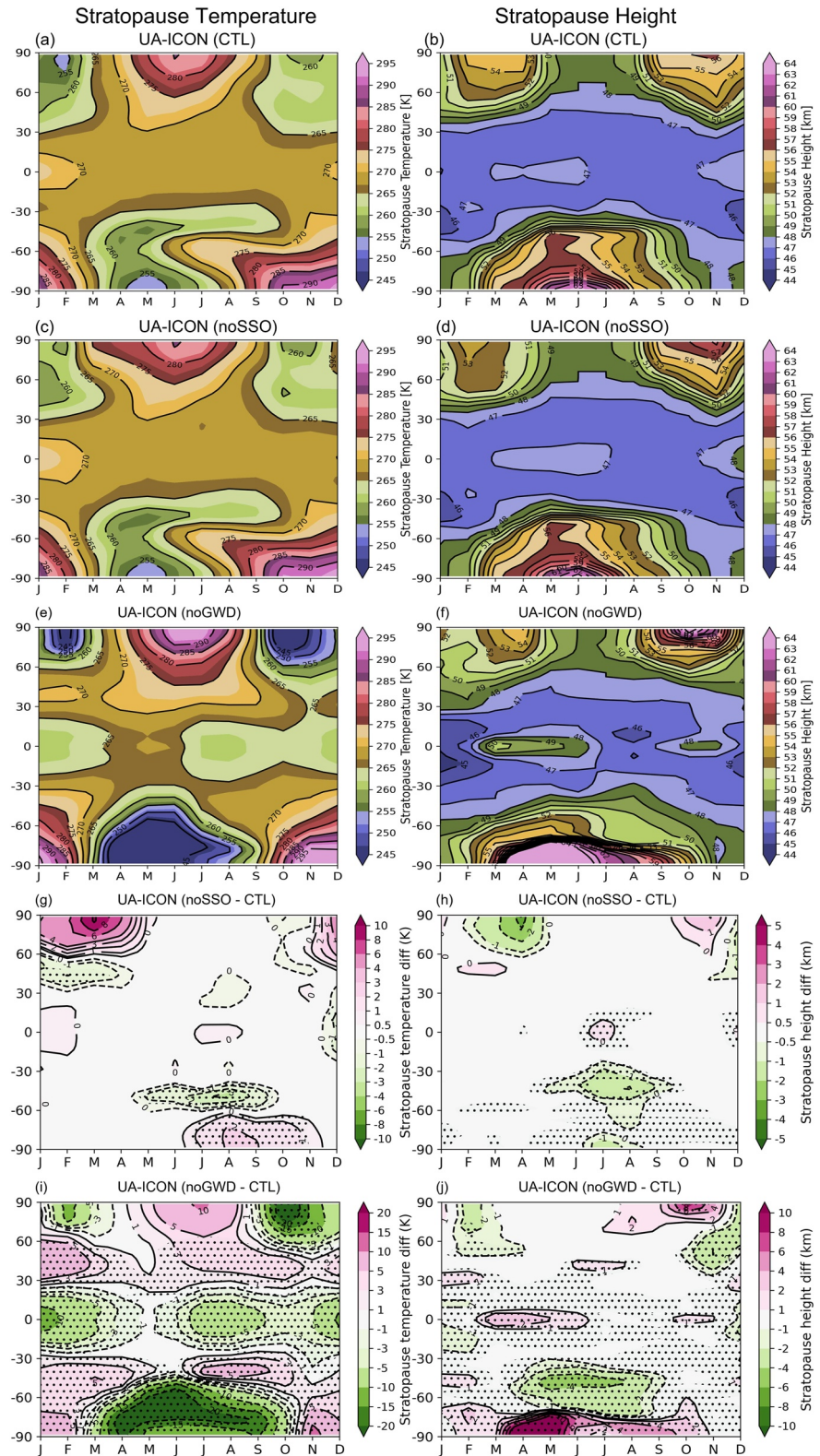


**Figure 4.** Latitude-time plot of the average annual cycle of stratopause temperature (left) and stratopause height (right). In CTL, both subgrid scale orographic and nonorographic gravity wave drags are used. In no-SSO and no-GWD, the subgrid scale orography and nonorographic gravity wave drags are switched off, respectively. The stippled areas in the two bottom rows indicate regions where the changes are statistically significant at 99% level according to the  $t$  test.

**Table 1**

*The Statistics of Major Sudden Stratospheric Warming Events (All SSWs), Elevated Stratopause Events (ESEs) and Major SSWs Not Followed by ESEs (SSW-Only) Events in the CTL and Sensitivity Runs With UA-ICON*

Model simulation	All SSWs	ESEs	SSWs-only
CTL	17 ( $\approx 57\%$ )	6 ( $\approx 20\%$ )	11 ( $\approx 36\%$ )
no-SSO	5 ( $\approx 17\%$ )	4 ( $\approx 13\%$ )	1 ( $\approx 3\%$ )
no-GWD	12 ( $\approx 40\%$ )	4 ( $\approx 13\%$ )	8 ( $\approx 27\%$ )

*Note.* The numbers in brackets indicate the percentage of winters out of the total for different events.

It is instructive to consider the dynamical mechanisms underlying the winters with ESEs and comparing it with winters with major SSWs but not followed by ESEs (SSW-only events). To this end we follow Chandran, Collins, et al. (2013) and examine the time evolution of composite maps of different variables around the occurrence of both types of events. The composites of the evolution of (a) zonal mean temperature, (b) zonal mean zonal wind, (c) Eliassen-Palm (EP) flux divergence, (d) total GW drag, (e) non-orographic GW drag, (f) SSO drag, (g) streamlines of the residual circulation, (h) the amplitude of the PWs for the zonal wavenumber 1 and (a) heat flux at 100 hPa for ES and SSW-only events in CTL simulation are presented in Figures 5 and 6, respectively. Their differences between ES and SSW-only events are shown in Figure 7. There is a subtle difference in the definition of day 0 between ES and SSW-only events. For the ESEs, day 0 is defined as the day of the stratopause height jump

based on the algorithm described in the previous section. However, for the SSW-only events, we chose day 0 as 11 days after the wind reversal at 10 hPa as on average ESEs occur 11 days after SSWs in CTL run. This enables a direct comparison of dynamical fields between ESEs and SSW-only events. In the study of Chandran, Collins, et al. (2013) and Scheffler et al. (2022), day 0 was chosen as 10 and 14 days after the wind reversal at 10 hPa, respectively. From the composite plots presented in Figures 5 and 6, we found some features that are listed below. These points broadly agree with previous studies with EMAC and WACCM (Chandran, Collins, et al., 2013; Limpasuvan et al., 2016; Scheffler et al., 2022), however, also some differences can be found. It is worthwhile to mention that generally the differences between ES and SSW-only events are not statistically significant.

In both ES and SSW-only events (Figures 5a and 6a, respectively), during (around day  $-11$ ) and after SSWs, the stratopause height (indicated by the green dots) drops before it reforms above the usual altitude. This reduction in the stratopause height during and shortly after SSWs is due to enhanced residual circulation at about 30–40 km around the SSWs occurrence day. The positive values of the residual circulation indicate a poleward and downward circulation. The enhancement in the altitude of the reformed stratopause is consistent with the stronger residual circulation at about 70–100 km around and after day 0 in both types of events, although the enhancement in the residual circulation around and after day 0 is stronger in ESEs compared to SSW-only events, as shown in Figure 7g. While there is a clear jump in the stratopause height following ES events, the reformed stratopause only weakly shifts upward during SSW-only events which is consistent with the previous studies (Chandran, Collins, et al., 2013; Scheffler et al., 2022). In general, following the SSWs, the stratosphere is colder in ES composites compared to the SSW-only around and after day 0 (Figure 7a). The negative temperature anomalies appear first at about 90 km around day  $-25$  and propagate downward and reach about 40 km around day  $+20$ . The stratopause returns to the altitudes before the SSW occurrence approximately at day  $+45$  in the SSW-only events but in the ESEs even around day  $+60$ , the stratopause is about a few kilometers above its altitude compared to the time before the SSWs.

The deceleration of the zonal mean zonal wind seems to be initiated from the mesosphere at about day  $-50$  and then propagates downward in both types of events. The wind reversal is stronger and long-lasting in the ESEs than in SSW-only events (Figure 7b) which differs from the study of Scheffler et al. (2022) who found that in the EMAC model the wind reversal is stronger in SSW-only events compared to ESEs. This might be due to the relatively small number of events considered in the present study and also in the study of Scheffler et al. (2022) and given a large wind variability during and around SSW onset, such differences between models are expected. The easterlies extend to the mesosphere (approximately up to about 80 km) in the composites of ESEs but the easterlies are limited to below 60 km in the case of SSW-only events. However, it is worthwhile to mention that the zonal mean zonal wind composites in both of these events presented in Figures 5 and 6b are averages of different events with different timing for the occurrence of SSWs. Moreover, here the 11 days is chosen as on average ESEs are detected 11 days after SSWs (between 5 and 19 days following SSW events). Such a varying time lag can cause the cancellation of positive and negative values of the zonal mean zonal wind and hence may lead to smaller values of positive and negative zonal mean zonal wind as well as a possible shorter duration of wind reversals (particularly in SSW-only events). For example, there is no SSW event in both SSW-only and ESEs with a wind reversal shorter than 5 days in the middle atmosphere at about 10 hPa.

In both types of events, the mesosphere cools during SSW events which is consistent with the anomalously weak residual circulation. It appears that only anomalies of non-orographic GW drag in this period are important for the mesospheric cooling and the role of EP drag is negligible in both types of events. In addition, the reformed zonal

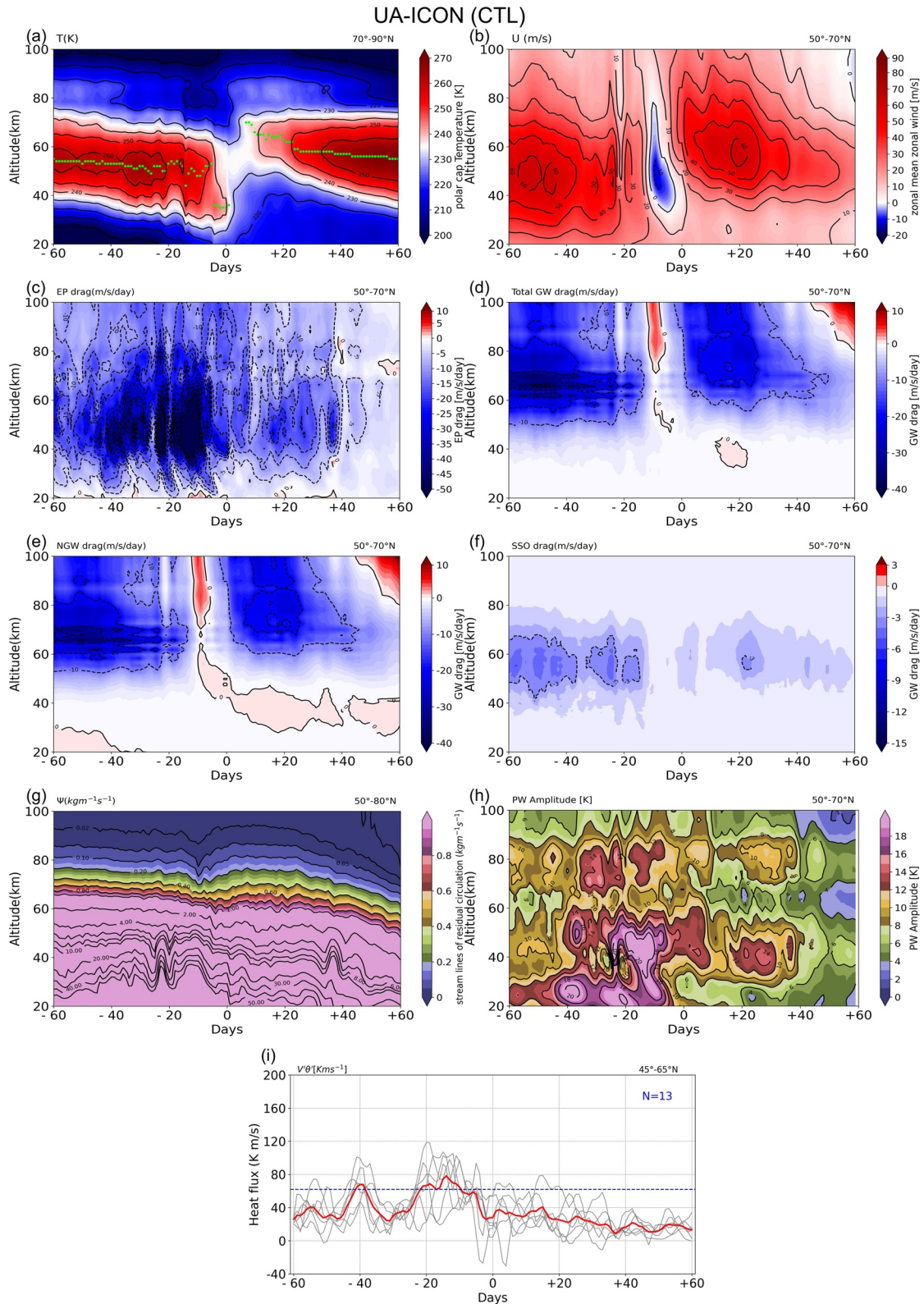


Figure 5.

mean zonal wind (Figures 5b and 6b) between day +5 and +35 is approximately 10–15 m/s stronger at 50–60 km in case of ESEs than for SSW-only events. The stronger reformed jet in ESEs compared to SSW-only events is consistent with the results of Scheffler et al. (2022) and Chandran, Collins, et al. (2013). The stronger westerly jet in ESEs compared to the SSWs-only events filters more eastward propagating GWs and hence during the same period (day +5 and +35) anomalously weaker eastward GW drag (or stronger westward GW drag) are found at about 60 km (SSO GW drag) and 60–100 km (non-orographic GW drag), respectively. Such anomalously stronger GW drag (shown in Figures 7d and 7e) during this period, explains the stronger residual circulation in the composites of ESEs compared to SSW-only events (Figure 7g).

Around the onset of ES and SSW-only events and shortly afterward, the planetary wave amplitude for the zonal wavenumber 1 weakens at upper stratosphere (Figures 5h and 6h). This is consistent with the Charney and Drazin (1961) that following the wind reversal in the stratosphere, the upward propagation of large-scale PWs from the troposphere to the middle atmosphere is hindered as wave propagation is only allowed when the background flow is westerly and weaker than a critical value. Note that as the wind reversal is weaker and shorter for the SSW-only composites, the reduction in the PW amplitudes after SSWs is also less noticeable compared to the ESEs. This is consistent with the reduced PW amplitudes in the stratosphere in the composites of ESEs compared to SSW-only events around and shortly after day 0 (Figure 7h).

Based on the differences in the EP flux divergence and GW drag presented in Figure 7, we suggest that the contributions of both GW and PW drag are important for the stronger residual circulation between 70 and 100 km following ESEs compared to the SSW-only events. Particularly between days –5 and +5 at about 60–100 km, the contributions from the PWs (Figure 7c) are important to explain the enhanced residual circulation in ESEs compared to SSW-only events. Between days +5 and +25, however, the enhanced residual circulation at about 70–100 km is due to the contributions from the GWs (Figures 7d and 7e). It is worthwhile to remind that the total (resolved EP flux and parameterized GW drags) wave forcing is largely balanced by the Coriolis term in the winter extra-tropical middle atmosphere (Hitchman et al., 1989) and therefore a westward drag implies a poleward and downward residual circulation.

The extra-tropical eddy heat flux which is a common measure for the penetration of the tropospheric waves from the troposphere to the stratosphere is presented (by the gray lines for each event and by the blue thick line for the climatology) in Figures 5i and 6i for the ES and SSW-only events, respectively. The number of days during which the heat fluxes exceed one standard deviation above the mean heat flux between day –60 and day 0 (indicated by the blue dashed line) is 13 and 6 days in the case of ES and SSW-only events, respectively. This is an indication of a relatively short but abrupt increase of eddy heat flux prior to the SSW onset in the case of SSW-only events. Instead, in the ESEs, there are two pulses of heat flux before the onset of wind before SSWs, where the second tropospheric pulse is more persistent and long-lasting than the SSW-only counterpart. Although, these results are similar to the results presented in Scheffler et al. (2022), nevertheless given the large variability of atmospheric fields during SSWs, a composite analysis with much more events are desirable to a better understanding if the ESEs are significantly differ from the SSW-only events.

### 3.4. Sensitivity of the ESEs to Absence of GW Drag

Similar to the previous section, the time evolution of composite maps of different variables around the occurrence of ESEs in no-SSO and no-GWD simulations are presented in Figures 8 and 9, respectively. Here we summarize the differences between the no-SSO and no-GWD simulations with the CTL run (Figure 5). This will help to understand how the absence of GWs affect the ESEs in UA-ICON. The differences between the no-SSO and no-GWD simulations compared to the CTL run are presented in Figures 10 and 11, respectively.

In the no-GWD simulation, the stratopause height drops around day –25 and then increases again before dropping again around day –10. The stratopause height reduction following ESEs around days –5 and 0 is less obvious for the no-GWD simulation compared to the CTL and no-SSO runs. The reformed stratopause around day

**Figure 5.** The Elevated stratopause (ES) events composites for the UA-ICON (CTL) simulation of (a) zonal mean temperature, (b) zonal mean zonal wind, (c) EP flux divergence, (d) total (non-orographic + SSO) GW drag, (e) non-orographic GW drag, (f) SSO GW drag, (g) the stream lines of the residual circulation, (h) PW amplitude for the zonal wavenumber  $k = 1$  and (i) heat flux at 100 hPa. On the abscissa, days are relative to the ESEs onset (i.e., day 0). On the top right of each panel, the latitudinal band used for averaging is shown. The green dots in (a) indicate the daily average stratopause height with an extra condition that the lapse rate must be at least 2 K between the level of maximum temperature and 4 levels (4 km) below and above it. The number of days during which the heat fluxes exceed one standard deviation above the mean heat flux between day –60 and day 0 in (i) is indicated by N and is shown by the dashed horizontal blue line. The colorbar in (g) is chosen to highlight the magnitude of the stream lines of residual circulation in the mesosphere.

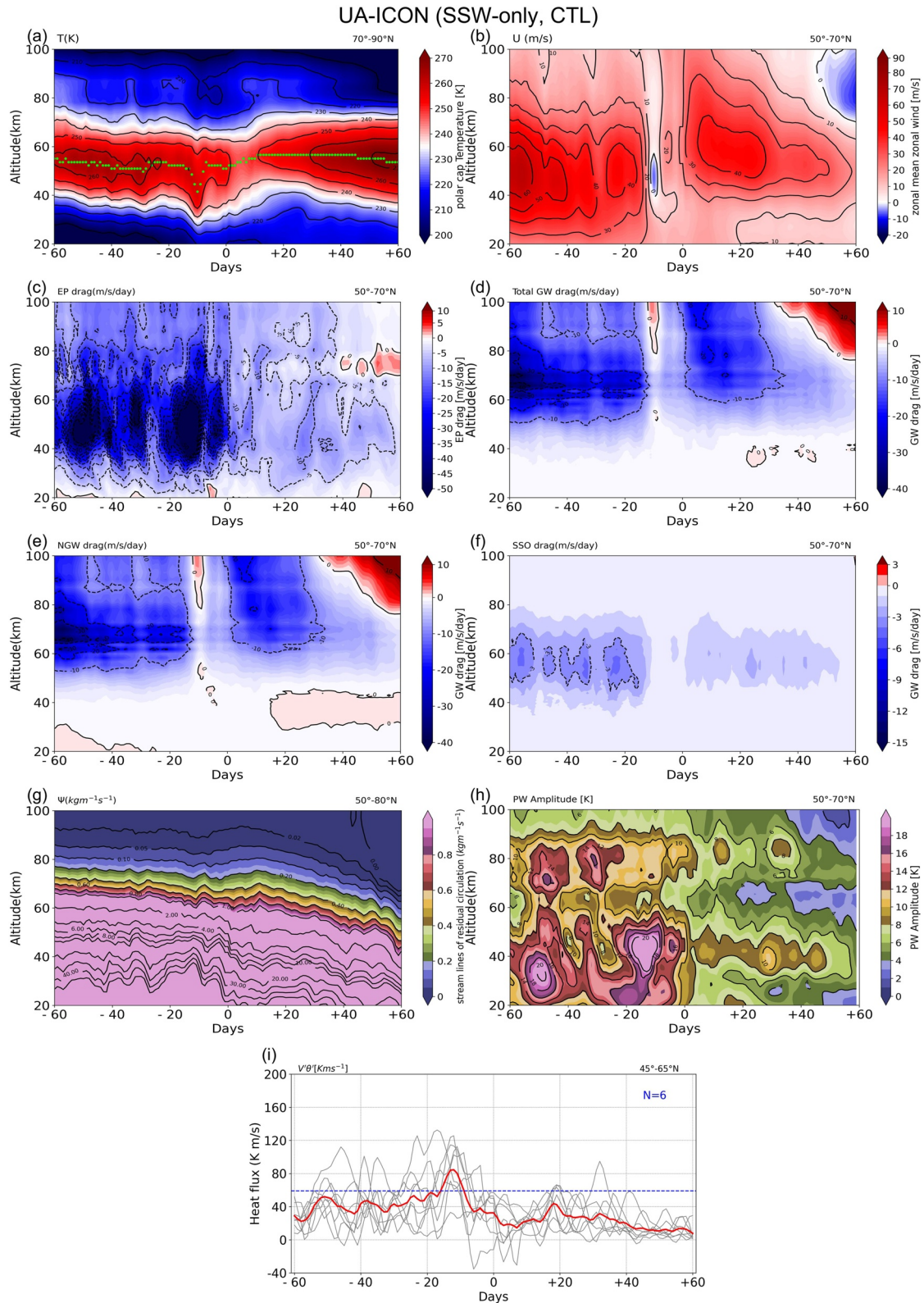


**Figure 6.** As Figure 5 but for SSWs not followed by ESEs.

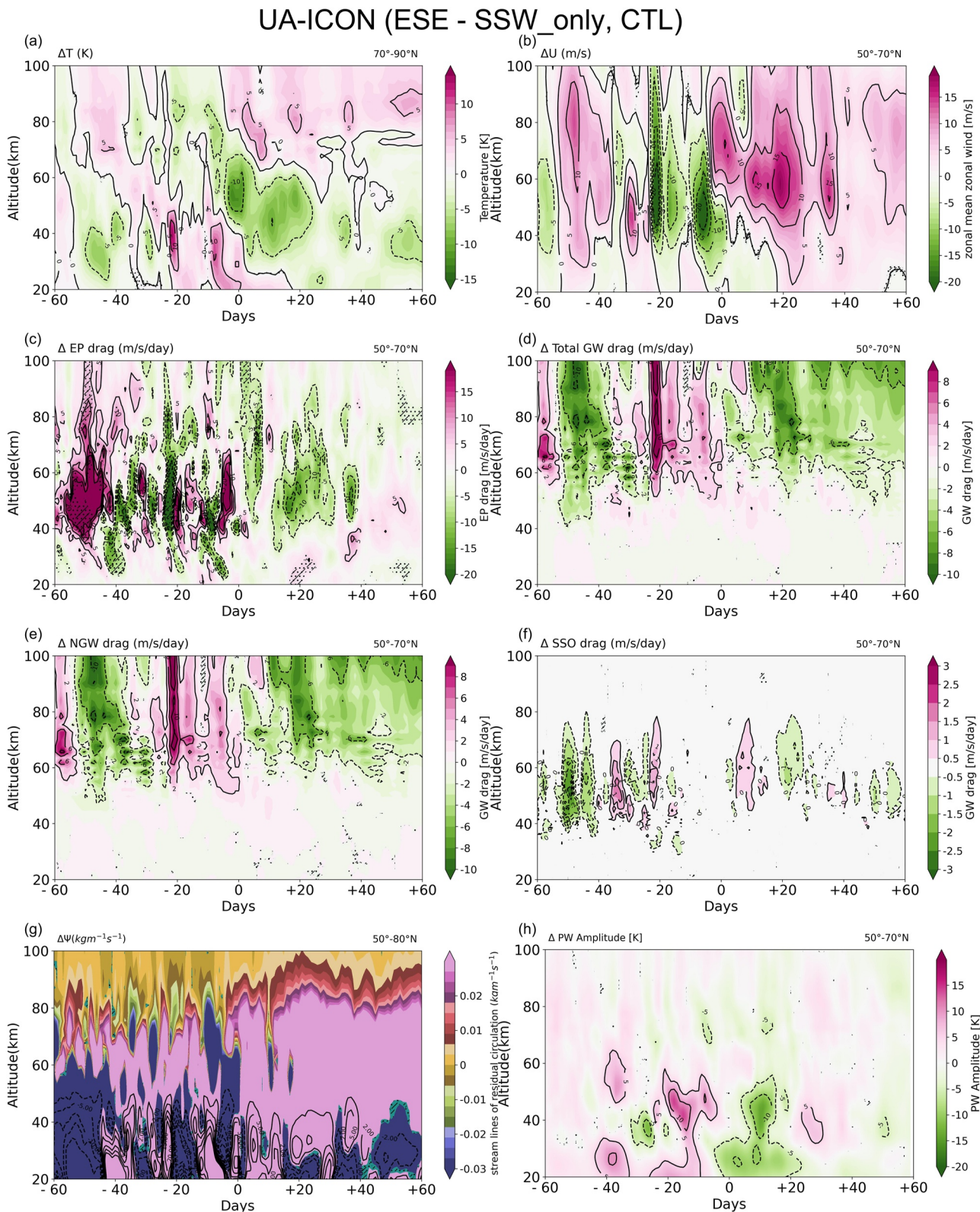


**Figure 7.** The differences in the variables between ESEs and SSWs not followed by ES events. The stippled and hatched areas indicate regions where p-values are less than 0.05 and 0.01, respectively.

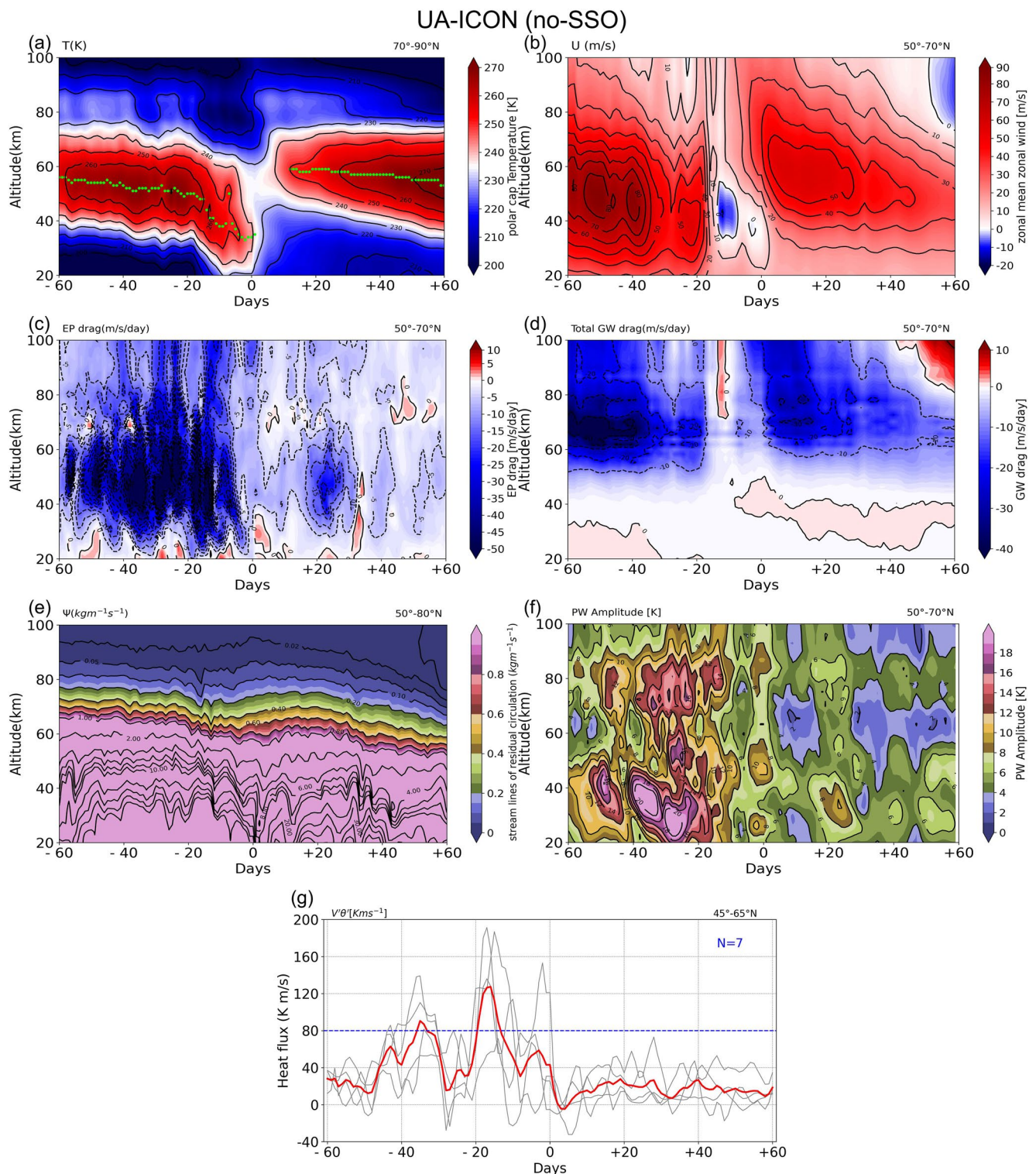


**Figure 8.** As Figure 5 but for the noSSO simulation. Note that the total GW drag presented in (d) equals to the drag by the non-orographic GWs as SSO drag is absent in the no-SSO simulation and therefore the GWD and SSO drags are not separately shown.

+5 is about 20 km higher than in CTL for the no-GWD simulation (it is detected at approximately 85 km) and drops to slightly above 60 km around day +15 (Figure 9a). The appearance of the elevated stratopause at a very high altitude in the no-GWD simulation is due to the anomalously weak residual circulation around days +10 and +15 that creates an anomalously low temperature between 60 and 80 km (Figure 11a) which is the altitude



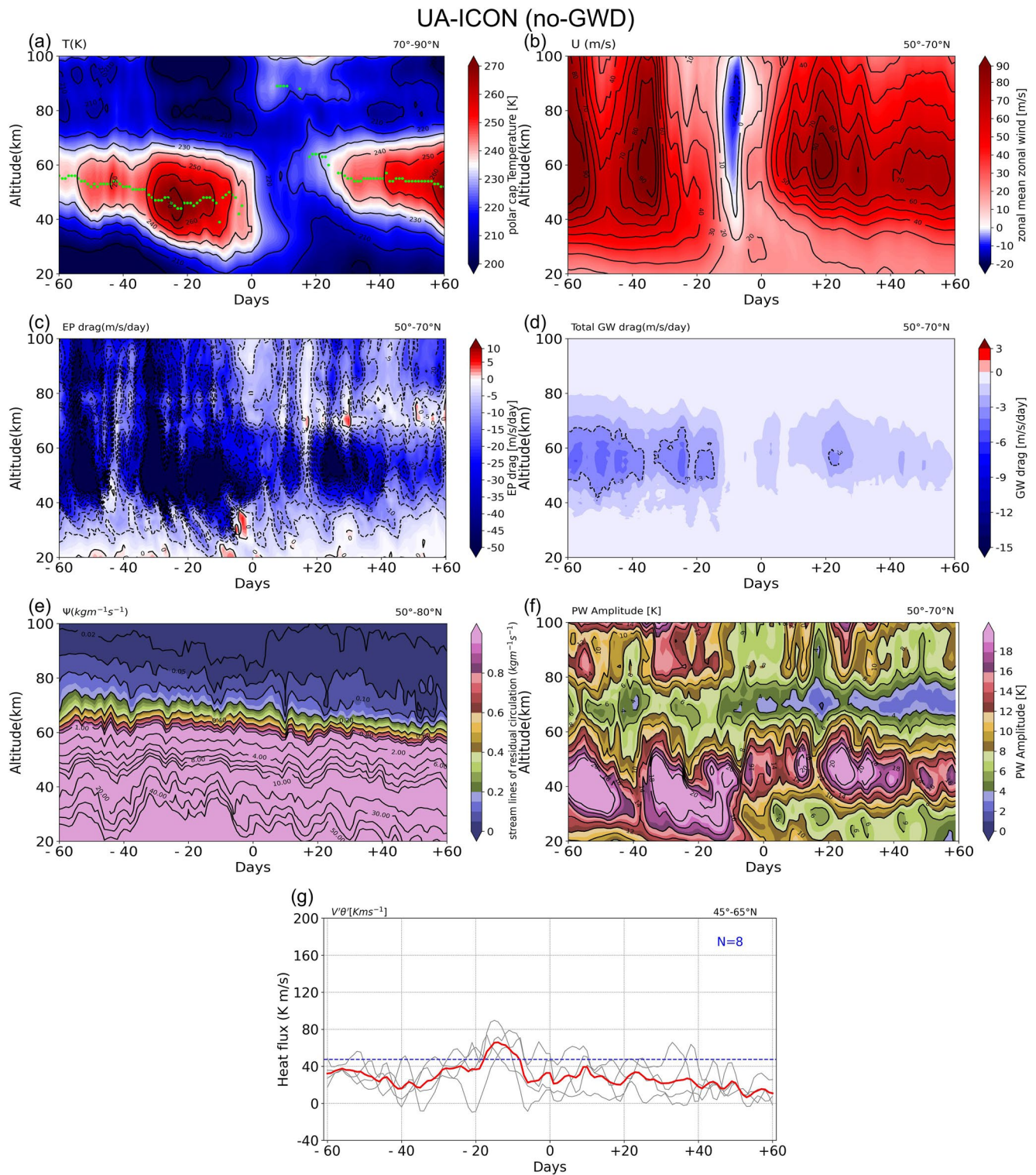


**Figure 9.** As Figure 5 but for the noGWD simulation. Note that the total GW drag presented in (d) equals to the drag by the SSO GWs as non-orographic drag is missing in no-GWD simulation and therefore the GWD and SSO drags are not separately shown.

range where the reformed stratopause is found in the CTL run. This is consistent with a weaker deposition of both GW and PW drags (Figures 11c and 11d, respectively) at about the same altitude and period range, although only the anomalies of GW drag are statistically significant. During the onset and after SSWs, the EP drag is anomalously weaker between 70 and 80 km (Figures 8c and 9c). Around day +15, strong EP drag appears above

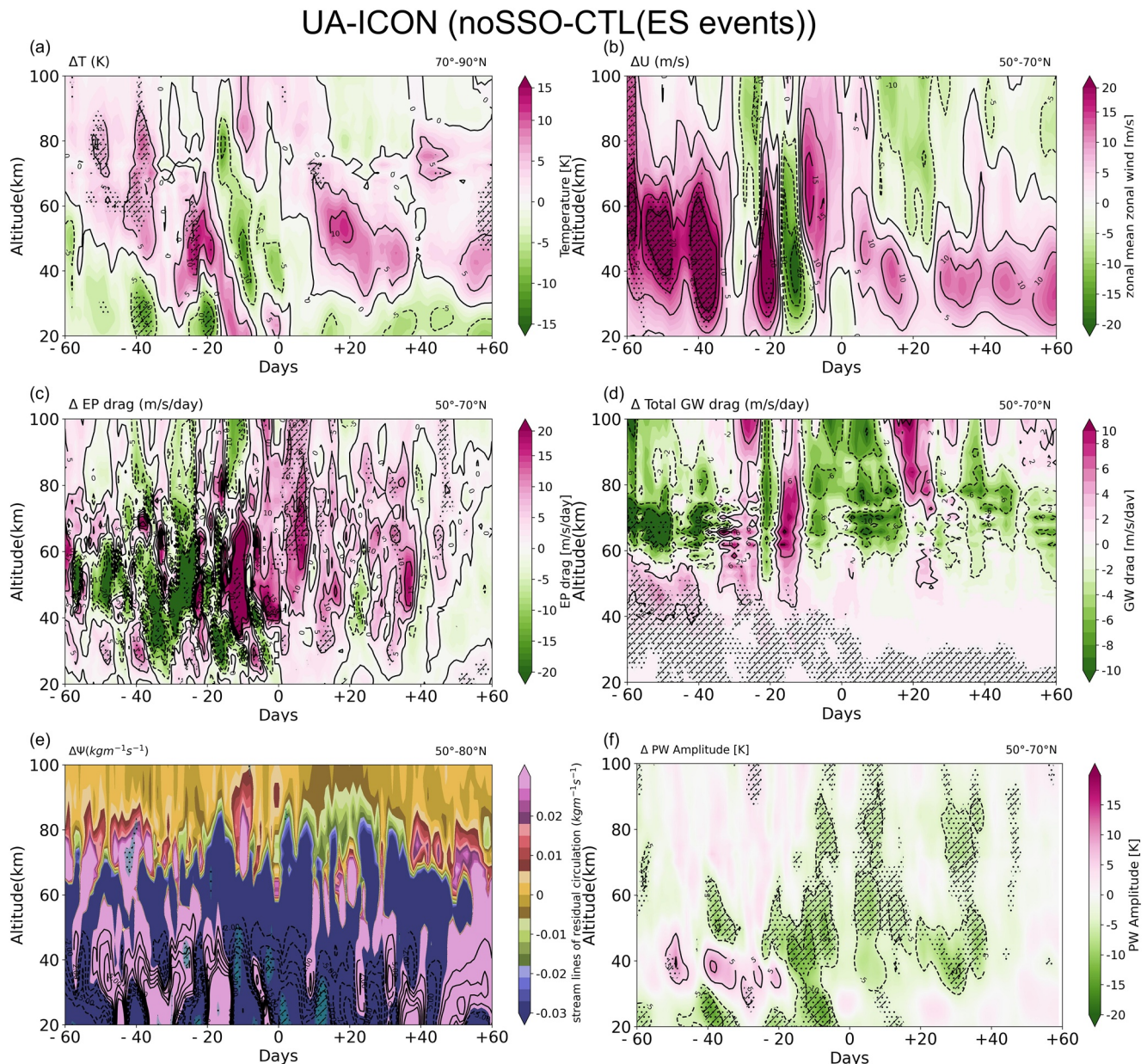


**Figure 10.** Differences between ESEs under no-SSO and CTL (noSSO-CTL) simulations. The stippled and hatched areas indicate regions where the changes are statistically significant at 90% and 95% levels according to the  $t$  test, respectively.

80 km (Figure 9c), which induces an enhancement of the residual circulation that gives rise to the formation of the elevated stratopause at about 85 km (Figure 9e). The appearance of the elevated stratopause in the no-GWD simulation is unexpected, as the contribution of total GWs is negligible above 80 km in the no-GWD simulation (Figure 7d) and it is the anomalous contributions from the resolved waves (e.g., EP flux drag) that give rise to the elevated stratopause. In other words, in the absence of GWs, the resolved wave drag acts to reform the elevated stratopause. While in the CTL simulation, an anomalous enhancement of the residual circulation (Figure 5g) is found at about 70–90 km after SSWs (between days 0 and 20), such enhancement of the residual circulation is absent in the no-GWD simulation. Instead, a noticeable enhancement of the residual circulation takes place above 90 km during the same period. Therefore, it can be concluded that not only GWD is crucial for the formation of ESEs, but the contributions from the resolved waves are important, too.

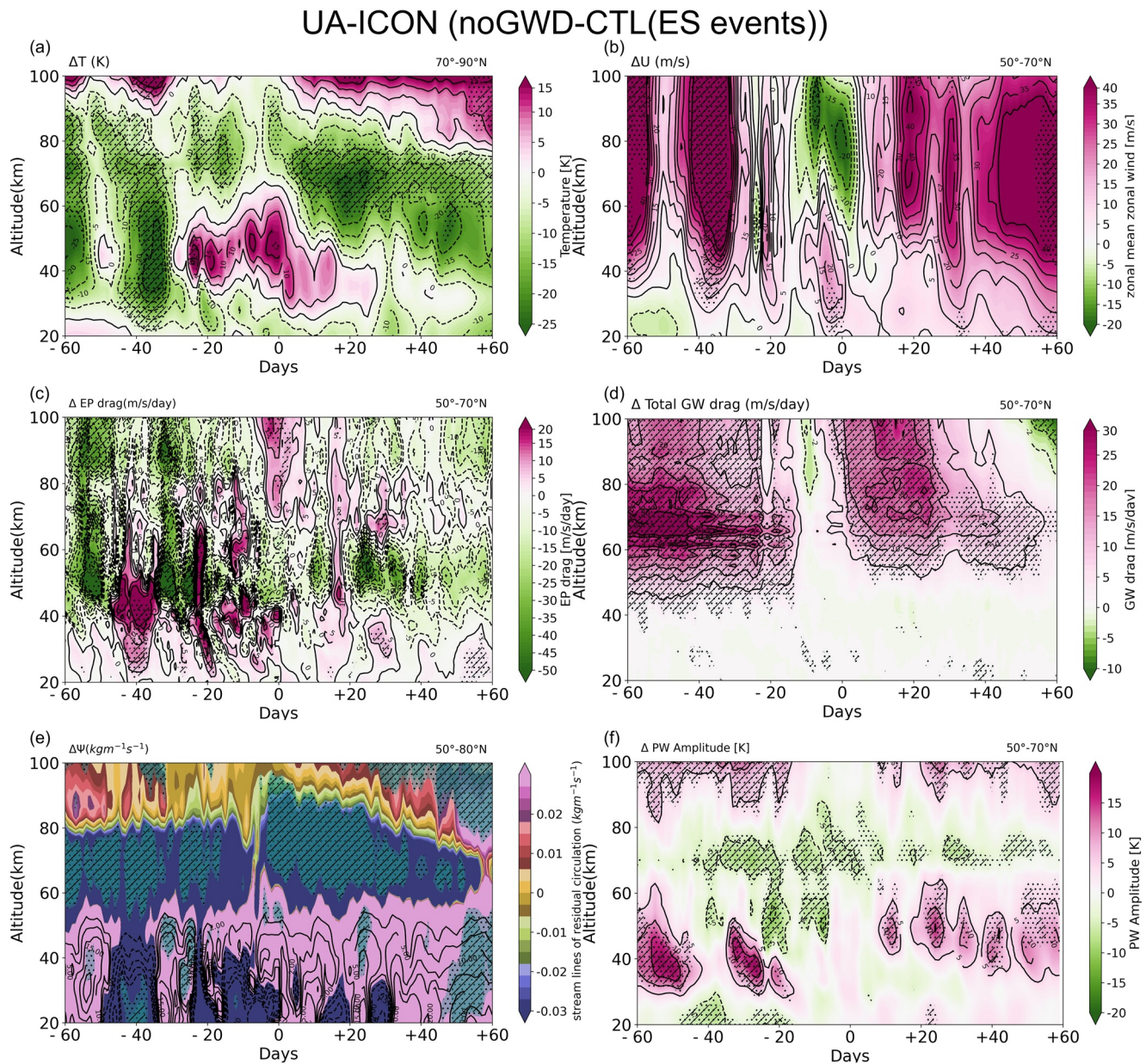


**Figure 11.** The same as Figure 8 but the differences are shown for the no-GWD and CTL (noGWD-CTL) simulations.

Without SSO drag, the reformed stratopause following ESEs appears approximately at 60 km (approximately 10 km lower than in the CTL simulation) around day +15. This is consistent with the anomalously weak residual circulation (Figure 10e) both in the stratosphere and mesosphere from days +5 to days +15. The total GW drag is stronger in the no-SSO simulation compared to CTL at approximately 60–100 km around days 0 and +20 (negative anomalies in Figure 10d), but the EP flux divergence is weaker in the no-SSO simulation compared to the CTL simulation (positive anomalies in Figure 10c) and the net wave action gives rise to the enhanced residual circulations in the CTL simulation at these altitudes, which helps to form the elevated stratopause at higher altitudes in the CTL compared to the no-SSO simulation. This suggests that the SSO drag is particularly important in the initial ES formation where the reformed ES typically forms at about 70 km in the CTL run, but excluding SSO drag leads to a reformed stratopause that appears approximately at 60 km.

The vertical extension of the reversed zonal wind is limited to approximately 50 km in the no-SSO run (Figure 8b) but in the no-GWD run, the decelerated zonal mean zonal wind is extended from about 40 to 100 km (Figure 9b).

Furthermore, in both no-SSO and no-GWD runs, stronger EP flux drag (Figures 10c and 11c) was found before the SSWs onset compared to the CTL run because the stronger winds before the events require stronger drags for the reversal of the zonal mean zonal winds.

The eddy heat flux composites in the no-SSO run are much more variable in the no-SSO simulation compared to the CTL and no-GWD simulations. The peak of the heat flux entering the stratosphere from the troposphere just before the SSWs onset is almost doubled in the no-SSO run compared to the CTL and no-GWD simulations.

#### 4. Summary, Discussion, and the Future Outlook

Using 17 years (2005–2021) of MLS observations, we first show the trends in the stratopause temperature and height in different seasons and regions. In general, the stratopause temperature and height trends indicated negative (cooling temperatures and decreasing heights) trends in most regions and seasons, although there are a few seasons or regions with positive trends. The largest negative trend in the stratopause temperature (by considering all regions and all seasons) is found in the SH's polar region in SON. The seasonal average of cooling rates is comparable in the mid-latitudes of NH and SH.

We also analyzed the monthly zonal-mean climatology of the stratopause temperature and height in the UA-ICON model (CLIM simulation) and compared it with a climatology based on MLS observations. Our results indicate that, in general, the UA-ICON model is able to realistically simulate the large-scale stratopause properties as compared to MLS observations in both hemispheres. Major differences between UA-ICON and MLS observations include the following:

1. The largest discrepancy between the UA-ICON model and MLS observations of stratopause temperature occurs during the cold months at high SH latitudes where the lowest stratopause temperatures in MLS are found between 45° and 60°S rather than southern polar latitudes found in UA-ICON climatology. This is due to the GW-driven descent and hence warming of the polar region that interrupts the cold winter stratopause in the SH. However, the coldest stratopause temperature in UA-ICON is found at the south pole during April–June and appears to be related to the weak GW-driven descent and hence warming in the mesosphere. In the study of France and Harvey (2013) the WACCM model has the largest bias in the stratopause properties in the Antarctic region similar to UA-ICON.
2. Although the tropical semiannual oscillation of the stratopause height and temperature are simulated in the UA-ICON, however, its timing differs from the MLS observations which is particularly noticeable in the stratopause height. While the maximum tropical stratopause heights are found during March–June and November–December in the UA-ICON simulation, in the MLS observation the maximum stratopause heights are found in January–February and July–August.

Next, we summarize the main results obtained from the sensitivity tests. Note that we mainly describe the response of the stratopause temperature to missing GWs because, in general, the stratopause temperature and height responses are synchronized. The higher stratopause is synchronized with the colder stratopause and vice versa.

1. As expected, the exclusion of SSO drag has negligible impact on the stratopause temperature in the low latitudes, however, the missing GWD induces statistically significant cooling in the tropical latitudes throughout the year. Due to the differences in the GW filtering by the zonal wind, the high-latitude responses of the stratopause temperatures to absence of SSO and GWD are different in sign (during cold months in both hemispheres, a positive/negative temperature anomaly are found for the no-SSO and no-GWD simulations, respectively).

Next, we summarize and discuss the main results of the ESEs analysis:

2. The frequency of SSWs is 5.7 events per decade in the CTL simulation and reduces to 1.7 and 4 events per decade in the no-SSO and no-GWD simulations, respectively. In the CTL simulation, the ESEs are detected on average 11 days after major SSWs. The ESEs occur in 20% of the boreal winters in the CTL simulation and reduce to 13% in both no-SSO and no-GWD simulations. Compared to previous studies (2.4 events per decade in EMCA (Scheffler et al., 2022), 2.8–3.6 events per decade in WACCM (Chandran, Collins, et al., 2013) and 3.5 events per decade in the MLS observations), our finding of 2 events per decade is lower but close to the frequencies of ESEs reported in these previous studies.

3. In both ES and SSW-only events, during and shortly after SSWs, the stratopause heights drop which is due to enhanced downward and equatorward residual circulation in the stratosphere. Consistent with the previous studies mentioned above, the reformed stratopause jumps to mesospheric altitudes only in the ESEs but in the SSW-only events, the reformed stratopause only weakly shifts upward compared to the periods before the SSWs occurrence. In general, the upper stratosphere and mesosphere are colder under ESEs shortly before and after ESEs compared to SSW-only events, and seems that the negative (cooling) temperature anomalies appear first at mesospheric altitudes around day  $-25$  and then propagate downward and reach about 40 km around day  $+20$ .
4. The wind reversal is stronger and long-lasting in the ESEs compared to SSW-only events. This is in agreement with the study of Chandran, Collins, et al. (2013) where they show that under ESEs stratospheric jet remains reversed longer than in those winters where an SSW occurs without an ES. In addition, the easterlies extend to the mesosphere in the composites of ESEs, but the reversed winds are limited to below 60 km in the case of SSW-only events.
5. Compared to the SSW-only events, the ESEs are triggered by more persistent heat flux injections from the troposphere which is also consistent with the long-lasting and stronger wind reversal in the stratosphere in the case of ESEs. This is in agreement with the results reported by Scheffler et al. (2022).

In the end, we summarize the major results of the elevated stratopause events in the UA-ICON under sensitivity simulations:

6. If the existence of the ESEs were only due to the anomalous residual circulation formed by the anomalies of the non-orographic GWs after SSWs, then one would expect the absence of ESEs under the no-GWD sensitivity test. However, this is not the case. The ESEs form even in the no-GWD sensitivity simulation, although they develop on average about 20 km higher compared to the CTL run. In this case, the anomalous residual circulation (Figure 9e) is due to the anomalously enhanced resolved wave forcing in the mesosphere that gives rise to the formation of the elevated stratopause at about 85 km. Although previous studies (Chandran, Garcia, et al., 2013; Limpasuvan et al., 2016; Okui et al., 2021) have shown that the EP flux divergence anomalies are important in the ES formation, our results show that even in the complete absence of GWD, the EP flux gives rise to the ES formation.
7. With the exclusion of SSO drag, the reformed stratopause is about 10 km lower than the reformed stratopause in the CTL simulation. This shows that the SSO drag is important particularly during the initial phase of ES formation.

The future outlook includes examining the individual contributions of traveling and stationary Rossby waves as well as resolved and parameterized gravity waves during ESEs. In addition, given the large variability in ES onset relative to SSW onset, the future research should consider a representative case study for both ES events and SSW-only events.

## Data Availability Statement

The ICON model code is distributed under a license issued by the Deutscher Wetterdienst (DWD) or Max Planck Institute for Meteorology (MPI-M). More information can be found at <https://code.mpimet.mpg.de/projects/icon-public>. The data used for the CTL (Karami & Jacobi, 2023a), noSSO (Karami & Jacobi, 2023c), and noGWD (Karami & Jacobi, 2023b) simulations are publicly available for download.

## References

- Barnett, J. J. (1974). The mean meridional temperature behaviour of the stratosphere from November 1970 to November 1971 derived from measurements by the selective chopper radiometer on nimbus iv. *Quarterly Journal of the Royal Meteorological Society*, *100*(426), 505–530. <https://doi.org/10.1002/qj.49710042602>
- Borchert, S., Zhou, G., Baldauf, M., Schmidt, H., Zängl, G., & Reinert, D. (2019). The upper-atmosphere extension of the icon general circulation model (version: UA-ICON-1.0). *Geoscientific Model Development*, *12*(8), 3541–3569. <https://doi.org/10.5194/gmd-12-3541-2019>
- Chandran, A., Collins, R., & Harvey, V. (2014). Stratosphere-mesosphere coupling during stratospheric sudden warming events. *Advances in Space Research*, *53*(9), 1265–1289. <https://doi.org/10.1016/j.asr.2014.02.005>
- Chandran, A., Collins, R. L., Garcia, R. R., Marsh, D. R., Harvey, V. L., Yue, J., & de la Torre, L. (2013). A climatology of elevated stratopause events in the whole atmosphere community climate model. *Journal of Geophysical Research: Atmospheres*, *118*(3), 1234–1246. <https://doi.org/10.1002/jgrd.50123>
- Chandran, A., Garcia, R. R., Collins, R. L., & Chang, L. C. (2013). Secondary planetary waves in the middle and upper atmosphere following the stratospheric sudden warming event of January 2012. *Geophysical Research Letters*, *40*(9), 1861–1867. <https://doi.org/10.1002/grl.50373>

## Acknowledgments

This study is funded by the Deutsche Forschungsgemeinschaft (DFG) under Grants JA 836/43, JA 836/47-1, and within the Transregional Collaborative Research Centre SFB/TRR 172 (Project-ID 268020496), subproject D01. PP and RE acknowledge support by GACR under Grants 21-20293J and 21-03295S. SB thanks the DFG for partial support through the research unit MS-GWaves and Grant ZA 268/10-2. This work used resources of the Deutsches Klimarechenzentrum (DKRZ) granted by its Scientific Steering Committee (WLA) under project ID bb1238. Khalil Karami thanks Haruka Okui and two other anonymous reviewers for reviewing our manuscript and providing the valuable comments.

- Charlton, A. J., & Polvani, L. M. (2007). A new look at stratospheric sudden warmings. Part I: Climatology and modeling benchmarks. *Journal of Climate*, 20(3), 449–469. <https://doi.org/10.1175/JCLI3996.1>
- Charney, J., & Drazin, P. (1961). Propagation of planetary-scale disturbances from the lower into the upper atmosphere. *Journal of Geophysical Research*, 66(1), 83–109. <https://doi.org/10.1029/JZ066i001p00083>
- de la Torre, L., Garcia, R. R., Barriopedro, D., & Chandran, A. (2012). Climatology and characteristics of stratospheric sudden warmings in the whole atmosphere community climate model. *Journal of Geophysical Research*, 117(D4), D04110. <https://doi.org/10.1029/2011JD016840>
- de Wit, R. J., Hibbins, R. E., Espy, P. J., Orsolini, Y. J., Limpasuvan, V., & Kinnison, D. E. (2014). Observations of gravity wave forcing of the mesopause region during the January 2013 major sudden stratospheric warming. *Geophysical Research Letters*, 41(13), 4745–4752. <https://doi.org/10.1002/2014GL060501>
- ECMWF. (2018). Part IV: Physical processes, chap. non-orographic gravity wave drag (pp. 69–74).
- Eichinger, R., Garny, H., Sácha, P., Danker, J., Dietmüller, S., & Oberländer-Hayn, S. (2020). Effects of missing gravity waves on stratospheric dynamics; Part I: Climatology. *Climate Dynamics*, 54(5), 3165–3183. <https://doi.org/10.1007/s00382-020-05166-w>
- France, J. A., & Harvey, V. L. (2013). A climatology of the stratopause in WACCM and the zonally asymmetric elevated stratopause. *Journal of Geophysical Research: Atmospheres*, 118(5), 2241–2254. <https://doi.org/10.1002/jgrd.50218>
- France, J. A., Harvey, V. L., Alexander, M. J., Randall, C. E., & Gille, J. C. (2012). High resolution dynamics limb sounder observations of the gravity wave-driven elevated stratopause in 2006. *Journal of Geophysical Research*, 117(D20), D20108. <https://doi.org/10.1029/2012JD017958>
- France, J. A., Harvey, V. L., Randall, C. E., Hitchman, M. H., & Schwartz, M. J. (2012). A climatology of stratopause temperature and height in the polar vortex and anticyclones. *Journal of Geophysical Research*, 117(D6), D06116. <https://doi.org/10.1029/2011JD016893>
- García, R. R., & Boville, B. A. (1994). Downward control of the mean meridional circulation and temperature distribution of the polar winter stratosphere. *Journal of the Atmospheric Sciences*, 51(15), 2238–2245. [https://doi.org/10.1175/1520-0469\(1994\)051<2238:COTMMC>2.0.CO;2](https://doi.org/10.1175/1520-0469(1994)051<2238:COTMMC>2.0.CO;2)
- Giorgetta, M. A., Brokopf, R., Crueger, T., Esch, M., Fiedler, S., Helmert, J., et al. (2018). Icon-s, the atmosphere component of the icon Earth system model: I. Model description. *Journal of Advances in Modeling Earth Systems*, 10(7), 1613–1637. <https://doi.org/10.1029/2017MS001242>
- Hitchman, M. H., Gille, J. C., Rodgers, C. D., & Brasseur, G. (1989). The separated polar winter stratopause: A gravity wave driven climatological feature. *Journal of the Atmospheric Sciences*, 46(3), 410–422. [https://doi.org/10.1175/1520-0469\(1989\)046<0410:TSPWSA>2.0.CO;2](https://doi.org/10.1175/1520-0469(1989)046<0410:TSPWSA>2.0.CO;2)
- Hitchman, M. H., & Leovy, C. B. (1986). Evolution of the zonal mean state in the equatorial middle atmosphere during October 1978–May 1979. *Journal of the Atmospheric Sciences*, 43(24), 3159–3176. [https://doi.org/10.1175/1520-0469\(1986\)043<0315:JAS>2.0.CO;2](https://doi.org/10.1175/1520-0469(1986)043<0315:JAS>2.0.CO;2)
- Holton, J. R. (1983). The influence of gravity wave breaking on the general circulation of the middle atmosphere. *Journal of the Atmospheric Sciences*, 40(10), 2497–2507. [https://doi.org/10.1175/1520-0469\(1983\)040<2497:TIOGWB>2.0.CO;2](https://doi.org/10.1175/1520-0469(1983)040<2497:TIOGWB>2.0.CO;2)
- Hood, L. L. (1986). Coupled stratospheric ozone and temperature responses to short-term changes in solar ultraviolet flux: An analysis of Nimbus 7 SBUV and SAMS data. *Journal of Geophysical Research*, 91(D4), 5264–5276. <https://doi.org/10.1029/JD091iD04p05264>
- Kanzawa, H. (1989). Warm stratopause in the Antarctic winter. *Journal of the Atmospheric Sciences*, 46(3), 435–438. [https://doi.org/10.1175/1520-0469\(1989\)046<0435:WSITAW>2.0.CO;2](https://doi.org/10.1175/1520-0469(1989)046<0435:WSITAW>2.0.CO;2)
- Karami, K., & Jacobi, C. (2023a). Upper atmosphere icon model time slice experiment under 1985 repeated 30 years R2B4 resolution control run [Dataset]. WDC. [https://doi.org/10.26050/WDC/UAICON\\_timesl\\_ctrl](https://doi.org/10.26050/WDC/UAICON_timesl_ctrl)
- Karami, K., & Jacobi, C. (2023b). Upper atmosphere icon model time slice experiment under 1985 repeated 30 years R2B4 resolution no nonorographic scale orographic gravity waves [Dataset]. WDC. [https://doi.org/10.26050/WDC/UAICON\\_timesl\\_nonon](https://doi.org/10.26050/WDC/UAICON_timesl_nonon)
- Karami, K., & Jacobi, C. (2023c). Upper atmosphere icon model time slice experiment under 1985 repeated 30 years R2B4 resolution no subgrid scale orographic gravity waves [Dataset]. WDC. [https://doi.org/10.26050/WDC/UAICON\\_timesl\\_nosso](https://doi.org/10.26050/WDC/UAICON_timesl_nosso)
- Karami, K., Mehrdad, S., & Jacobi, C. (2022). Response of the resolved planetary wave activity and amplitude to turned off gravity waves in the UA-ICON general circulation model. *Journal of Atmospheric and Solar-Terrestrial Physics*, 241, 105967. <https://doi.org/10.1016/j.jastp.2022.105967>
- Köhler, R., Handorf, D., Jaiser, R., Dethloff, K., Zängl, G., Majewski, D., & Rex, M. (2021). Improved circulation in the northern hemisphere by adjusting gravity wave drag parameterizations in seasonal experiments with icon-NWP. *Earth and Space Science*, 8(3), e2021EA001676. <https://doi.org/10.1029/2021EA001676>
- Kuilman, M. S., & Karlsson, B. (2018). The role of the winter residual circulation in the summer mesopause regions in WACCM. *Atmospheric Chemistry and Physics*, 18(6), 4217–4228. <https://doi.org/10.5194/acp-18-4217-2018>
- Kvissel, O.-K., Orsolini, Y. J., Stordal, F., Limpasuvan, V., Richter, J., & Marsh, D. R. (2012). Mesospheric intrusion and anomalous chemistry during and after a major stratospheric sudden warming. *Journal of Atmospheric and Solar-Terrestrial Physics*, 78–79, 116–124. <https://doi.org/10.1016/j.jastp.2011.08.015>
- Labitzke, K. (1972). Temperature changes in the mesosphere and stratosphere connected with circulation changes in winter. *Journal of the Atmospheric Sciences*, 29(4), 756–766. [https://doi.org/10.1175/1520-0469\(1972\)029<0756:TCITMA>2.0.CO;2](https://doi.org/10.1175/1520-0469(1972)029<0756:TCITMA>2.0.CO;2)
- Labitzke, K. (1981a). The amplification of height wave 1 in January 1979: A characteristic precondition for the major warming in February. *Monthly Weather Review*, 109(5), 983–989. [https://doi.org/10.1175/1520-0493\(1981\)109<0983:TAOHWI>2.0.CO;2](https://doi.org/10.1175/1520-0493(1981)109<0983:TAOHWI>2.0.CO;2)
- Labitzke, K. (1981b). Stratospheric-mesospheric midwinter disturbances: A summary of observed characteristics. *Journal of Geophysical Research*, 86(C10), 9665–9678. <https://doi.org/10.1029/JC086iC10p09665>
- Limpasuvan, V., Orsolini, Y. J., Chandran, A., Garcia, R. R., & Smith, A. K. (2016). On the composite response of the MLT to major sudden stratospheric warming events with elevated stratopause. *Journal of Geophysical Research: Atmospheres*, 121(9), 4518–4537. <https://doi.org/10.1002/2015JD024401>
- Liu, H.-L., & Roble, R. G. (2002). A study of a self-generated stratospheric sudden warming and its mesospheric–lower thermospheric impacts using the coupled time-GCM/CCM3. *Journal of Geophysical Research*, 107(D23), ACL15–1–ACL15–18. <https://doi.org/10.1029/2001JD001533>
- Lott, F., & Miller, M. J. (1997). A new subgrid-scale orographic drag parameterization: Its formulation and testing. *Quarterly Journal of the Royal Meteorological Society*, 123(537), 101–127. <https://doi.org/10.1002/qj.49712353704>
- Manney, G. L., Krüger, K., Pawson, S., Minschwaner, K., Schwartz, M. J., Daffer, W. H., et al. (2008). The evolution of the stratopause during the 2006 major warming: Satellite data and assimilated meteorological analyses. *Journal of Geophysical Research*, 113(D11), D11115. <https://doi.org/10.1029/2007JD009097>
- Manney, G. L., Krüger, K., Sabutis, J. L., Sena, S. A., & Pawson, S. (2005). The remarkable 2003–2004 winter and other recent warm winters in the arctic stratosphere since the late 1990s. *Journal of Geophysical Research*, 110(D4), D04107. <https://doi.org/10.1029/2004JD005367>
- McLandress, C., Scinocca, J. F., Shepherd, T. G., Reader, M. C., & Manney, G. L. (2013). Dynamical control of the mesosphere by orographic and nonorographic gravity wave drag during the extended northern winters of 2006 and 2009. *Journal of the Atmospheric Sciences*, 70(7), 2152–2169. <https://doi.org/10.1175/JAS-D-12-0297.1>
- Meinshausen, M., Vogel, E., Nauels, A., Lorbacher, K., Meinshausen, N., Etheridge, D. M., et al. (2017). Historical greenhouse gas concentrations for climate modelling (CMIP6). *Geoscientific Model Development*, 10(5), 2057–2116. <https://doi.org/10.5194/gmd-10-2057-2017>

- Naren Athreyas, K., Garcia, R., & Chandran, A. (2022). Inter-hemispheric coupling during sudden stratospheric warming events with elevated stratopause. *Journal of Geophysical Research: Atmospheres*, 127(1), e2020JD033761. <https://doi.org/10.1029/2020JD033761>
- Okui, H., Sato, K., Koshin, D., & Watanabe, S. (2021). Formation of a mesospheric inversion layer and the subsequent elevated stratopause associated with the major stratospheric sudden warming in 2018/19. *Journal of Geophysical Research: Atmospheres*, 126(18), e2021JD034681. <https://doi.org/10.1029/2021JD034681>
- Olivero, J., & Thomas, G. (2001). Evidence for changes in greenhouse gases in the mesosphere. *Advances in Space Research*, 28(7), 931–936. [https://doi.org/10.1016/S0273-1177\(01\)80020-X](https://doi.org/10.1016/S0273-1177(01)80020-X)
- Orsolini, Y. J., Limpasuvan, V., Pérot, K., Espy, P., Hibbins, R., Lossow, S., et al. (2017). Modelling the descent of nitric oxide during the elevated stratopause event of January 2013. *Journal of Atmospheric and Solar-Terrestrial Physics*, 155, 50–61. <https://doi.org/10.1016/j.jastp.2017.01.006>
- Orsolini, Y. J., Urban, J., Murtagh, D. P., Lossow, S., & Limpasuvan, V. (2010). Descent from the polar mesosphere and anomalously high stratopause observed in 8 years of water vapor and temperature satellite observations by the Odin sub-millimeter radiometer. *Journal of Geophysical Research*, 115(D12), D12305. <https://doi.org/10.1029/2009JD013501>
- Pisofit, P., Sacha, P., Polvani, L. M., Añel, J. A., de la Torre, L., Eichinger, R., et al. (2021). Stratospheric contraction caused by increasing greenhouse gases. *Environmental Research Letters*, 16(6), 064038. <https://doi.org/10.1088/1748-9326/abfe2b>
- Randall, C. E., Harvey, V. L., Manney, G. L., Orsolini, Y., Codrescu, M., Sioris, C., & Russell, J. M., III. (2005). Stratospheric effects of energetic particle precipitation in 2003–2004. *Geophysical Research Letters*, 32(5), L05802. <https://doi.org/10.1029/2004GL022003>
- Randall, C. E., Harvey, V. L., Siskind, D. E., France, J., Bernath, P. F., Boone, C. D., & Walker, K. A. (2009). Nox descent in the arctic middle atmosphere in early 2009. *Geophysical Research Letters*, 36(18), L18811. <https://doi.org/10.1029/2009GL039706>
- Ren, S., Polavarapu, S., Beagley, S. R., Nezhlin, Y., & Rochon, Y. J. (2011). The impact of gravity wave drag on mesospheric analyses of the 2006 stratospheric major warming. *Journal of Geophysical Research*, 116(D19), D19116. <https://doi.org/10.1029/2011JD015943>
- Rind, D., Shindell, D., Lonergan, P., & Balachandran, N. K. (1998). Climate change and the middle atmosphere. part iii: The doubled CO<sub>2</sub> climate revisited. *Journal of Climate*, 11(5), 876–894. [https://doi.org/10.1175/1520-0442\(1998\)011<0876:CCATMA>2.0.CO;2](https://doi.org/10.1175/1520-0442(1998)011<0876:CCATMA>2.0.CO;2)
- Sassi, F., Garcia, R. R., Boville, B. A., & Liu, H. (2002). On temperature inversions and the mesospheric surf zone. *Journal of Geophysical Research*, 107(D19), ACL8-1–ACL8-11. <https://doi.org/10.1029/2001JD001525>
- Scheffler, J., Ayarzagüena, B., Orsolini, Y. J., & Langematz, U. (2022). Elevated stratopause events in the current and a future climate: A chemistry-climate model study. *Journal of Atmospheric and Solar-Terrestrial Physics*, 227, 105804. <https://doi.org/10.1016/j.jastp.2021.105804>
- Schröder, T. M., Ao, C. O., & de la Torre Juárez, M. (2007). Sensitivity of GPS occultation to the stratopause height. *Journal of Geophysical Research*, 112(D6), D06119. <https://doi.org/10.1029/2006JD007330>
- Schwartz, M., Livesey, N., Read, W., & R, F. (2020). MLS/aura level 3 daily binned temperature on assorted grids v004, greenbelt, MD, USA, Goddard Earth sciences data and information services center (GES disc). <https://doi.org/10.5067/Aura/MLS/DATA/3121>
- Scinocca, J. F. (2003). An accurate spectral nonorographic gravity wave drag parameterization for general circulation models. *Journal of the Atmospheric Sciences*, 60(4), 667–682. [https://doi.org/10.1175/1520-0469\(2003\)060<0667:AASNGW>2.0.CO;2](https://doi.org/10.1175/1520-0469(2003)060<0667:AASNGW>2.0.CO;2)
- Shi, Y., Evtushevsky, O., Milinevsky, G., Klekociuk, A., Han, W., Ivaniha, O., et al. (2022). Zonal asymmetry of the stratopause in the 2019/2020 arctic winter. *Remote Sensing*, 14(6), 1496. <https://doi.org/10.3390/rs14061496>
- Siskind, D. E., Eckermann, S. D., Coy, L., McCormack, J. P., & Randall, C. E. (2007). On recent interannual variability of the arctic winter mesosphere: Implications for tracer descent. *Geophysical Research Letters*, 34(9), L09806. <https://doi.org/10.1029/2007GL029293>
- Siskind, D. E., Eckermann, S. D., McCormack, J. P., Coy, L., Hoppel, K. W., & Baker, N. L. (2010). Case studies of the mesospheric response to recent minor, major, and extended stratospheric warmings. *Journal of Geophysical Research*, 115(D3), D00N03. <https://doi.org/10.1029/2010JD014114>
- Siskind, D. E., Sassi, F., Randall, C. E., Harvey, V. L., Hervig, M. E., & Bailey, S. M. (2015). Is a high-altitude meteorological analysis necessary to simulate thermosphere-stratosphere coupling? *Geophysical Research Letters*, 42(19), 8225–8230. <https://doi.org/10.1002/2015GL065838>
- Smith, A. K., López-Puertas, M., García-Comas, M., & Tukiainen, S. (2009). SABER observations of mesospheric ozone during NH late winter 2002–2009. *Geophysical Research Letters*, 36(23), L23804. <https://doi.org/10.1029/2009GL040942>
- Steiner, A. K., Ladstädter, F., Randel, W. J., Maycock, A. C., Fu, Q., Claud, C., et al. (2020a). Observed temperature changes in the troposphere and stratosphere from 1979 to 2018. *Journal of Climate*, 33(19), 8165–8194. <https://doi.org/10.1175/JCLI-D-19-0998.1>
- Steiner, A. K., Ladstädter, F., Randel, W. J., Maycock, A. C., Fu, Q., Claud, C., et al. (2020b). Observed temperature changes in the troposphere and stratosphere from 1979 to 2018. *Journal of Climate*, 33(19), 8165–8194. <https://doi.org/10.1175/JCLI-D-19-0998.1>
- Taylor, K. E., Williamson, D., & Zwiers, F. (2000). The sea surface temperature and sea-ice concentration boundary conditions for AMIP II simulations. In *Program for climate model Diagnosis and Intercomparison*.
- Thuraiajah, B., Bailey, S. M., Cullens, C. Y., Hervig, M. E., & Russell, J. M., III. (2014). Gravity wave activity during recent stratospheric sudden warming events from Sofie temperature measurements. *Journal of Geophysical Research: Atmospheres*, 119(13), 8091–8103. <https://doi.org/10.1002/2014JD021763>
- Tomikawa, Y., Sato, K., Watanabe, S., Kawatani, Y., Miyazaki, K., & Takahashi, M. (2012). Growth of planetary waves and the formation of an elevated stratopause after a major stratospheric sudden warming in a T2131256 GCM. *Journal of Geophysical Research*, 117(D16). <https://doi.org/10.1029/2011JD017243>
- Tweedy, O. V., Limpasuvan, V., Orsolini, Y. J., Smith, A. K., Garcia, R. R., Kinnison, D., et al. (2013). Nighttime secondary ozone layer during major stratospheric sudden warmings in specified-dynamics WACCM. *Journal of Geophysical Research: Atmospheres*, 118(15), 8346–8358. <https://doi.org/10.1002/jgrd.50651>
- Warner, C. D., & McIntyre, M. E. (1996). On the propagation and dissipation of gravity wave spectra through a realistic middle atmosphere. *Journal of the Atmospheric Sciences*, 53(22), 3213–3235. [https://doi.org/10.1175/1520-0469\(1996\)053<3213:OTPADO>2.0.CO;2](https://doi.org/10.1175/1520-0469(1996)053<3213:OTPADO>2.0.CO;2)
- Waters, J. W., Froidevaux, L., Harwood, R. S., Jarnot, R. F., Pickett, H. M., Read, W. G., et al. (2006). The Earth observing system microwave limb sounder (EOS MLS) on the aura satellite. *IEEE Transactions on Geoscience and Remote Sensing*, 44(5), 1075–1092. <https://doi.org/10.1109/tgrs.2006.873771>
- Wehrbein, W. M., & Leovy, C. B. (1982). An accurate radiative heating and cooling algorithm for use in a dynamical model of the middle atmosphere. *Journal of the Atmospheric Sciences*, 39(7), 1532–1544. [https://doi.org/10.1175/1520-0469\(1982\)039<1532:AARHAC>2.0.CO;2](https://doi.org/10.1175/1520-0469(1982)039<1532:AARHAC>2.0.CO;2)
- Yamashita, C., Liu, H.-L., & Chu, X. (2010). Responses of mesosphere and lower thermosphere temperatures to gravity wave forcing during stratospheric sudden warming. *Geophysical Research Letters*, 37(9), L09803. <https://doi.org/10.1029/2009GL042351>
- Yiğit, E., & Medvedev, A. S. (2016). Role of gravity waves in vertical coupling during sudden stratospheric warmings. *Geoscience Letters*, 3(1), 1–13. <https://doi.org/10.1186/s40562-016-0056-1>
- Zängl, G., Reinert, D., Rípodas, P., & Baldauf, M. (2015). The icon (icosahedral non-hydrostatic) modelling framework of DWD and MPI-M: Description of the non-hydrostatic dynamical core. *Quarterly Journal of the Royal Meteorological Society*, 141(687), 563–579. <https://doi.org/10.1002/qj.2378>